arXiv:2012.00019v2 [astro-ph.GA] 26 Mar 2021

MNRAS 000, 1–23 (2020) Preprint 29 March 2021 Compiled using MNRAS LaTeX style file v3.0

On the duration of the embedded phase of star formation

Jaeyeon Kim,[1★] Mélanie Chevance,[1] J. M. Diederik Kruijssen,[1] Andreas Schruba,[2] Karin Sandstrom,[3] Ashley T. Barnes,[1] Frank Bigiel,[3] Guillermo A. Blanc,[5,6] Yixian Cao,[7] Daniel A. Dale,[8] Christopher M. Faesi,[9] Simon C. O. Glover,[10] Kathryn Grasha,[11] Brent Groves,[12] Cinthya Herrera,[13] Ralf S. Klessen,[10,14] Kathryn Kreckel,[7] Janice C. Lee,[15] Adam K. Leroy,[16] Jérôme Pety,[13,17] Miguel Querejeta,[18] Eva Schinnerer,[19] Jiayi Sun,[15] Antonio Usero,[18] Jacob L. Ward,[1] Thomas G. Williams[19]

Affiliations are listed at the end of the paper

Accepted Xxxxx XX. Received Xxxxx XX; in original form 2020 November 30

ABSTRACT

Feedback from massive stars plays a key role in molecular cloud evolution. After the onset of star formation, the young stellar population is exposed by photoionization, winds, supernovae, and radiation pressure from massive stars. Recent observations of nearby galaxies have provided the evolutionary timeline between molecular clouds and exposed young stars, but the duration of the embedded phase of massive star formation is still ill-constrained. We measure how long massive stellar populations remain embedded within their natal cloud by applying a statistical method to six nearby galaxies at 20−100 pc resolution using CO, *Spitzer* 24 μm, and Hα emission as tracers of molecular clouds, embedded star formation, and exposed star formation, respectively. We find that the embedded phase with CO and 24 μm emission lasts for 2−7 Myr and constitutes 17−47% of the cloud lifetime. During approximately the first half of this phase, the region is invisible in Hα, making it heavily obscured. For the second half of this phase, the region is emitting in Hα and is partially exposed. Once the cloud has been dispersed by feedback, 24 μm emission no longer traces ongoing star formation, but remains detectable for another 2−5 Myr through the emission from ambient CO-dark gas tracing star formation that recently ended. The short duration of massive star formation suggests that pre-supernova feedback, photoionization, and winds is important in disrupting molecular clouds. The measured timescales do not show significant correlations with environmental properties (e.g. metallicity). Future JWST observations will enable these measurements routinely across the nearby galaxy population.

Key words: stars: formation ; ISM: clouds ; galaxies: evolution ; galaxies: ISM ; galaxies: star formation

1 INTRODUCTION

Massive stars (≳ 8 M⊙) form in the densest regions of molecular clouds. Once formed, these stars emit large quantities of ionizing photons, creating H II regions, and generate strong winds, which in turn alter the structure of their natal clouds and the surrounding interstellar medium. After a relatively short lifetime (≲ 5 Myr; Leitherer & Heckman 1995; Eldridge et al. 2017; Gossage et al. 2019), these massive stars die in supernova explosions, injecting energy and momentum into their surroundings. Theoretical studies of giant molecular clouds (GMCs) indicate that these feedback processes are responsible for regulating the formation of stars from their parental clouds and destroying the GMCs (see, e.g. Krumholz 2014; Dale 2015; Chevance et al. 2020b, for recent reviews). However, it is still debated which feedback mechanisms efficiently disrupt the parti-

★ E-mail: kim@uni-heidelberg.de

© 2020 The Authors

clouds and which affect the diffuse interstellar medium on large scales (e.g. Lucas et al. 2020; A. Barnes et al. in preparation).

Observationally, several studies have constrained the timescale of GMC destruction by stellar feedback in the Milky Way and in nearby galaxies using optical and UV star formation tracers, which are sensitive to recent, not heavily obscured star formation. Kapsi dispersion of GMCs within a cloud (dynamical timescale, ≲ 10 Myr) has been suggested based on the spatial distributions of stars in nearby star-forming regions and young stellar associations (Efremov 1995; Hartmann 2001) for GMCs in the Milky Way, M33, and the Large Magellanic Cloud (LMC) (somewhat longer feedback timescales, ≳ 10 − 30 Myr) have been proposed by classifying molecular clouds into different types based on the non-existence of their star formation activity (Engargiola et al. 2003; Blitz et al. 2007; Kawamura et al. 2009; Miura et al. 2012; Corbelli et al. 2017). Such methods have limitations because individual GMCs and star-forming regions need to be resolved

the analysis of mid-CO and far emission. The duration of the embedded phase of massive star formation (i.e. feedback timescale $\tau_{\rm feedback}$) which continues until disruption of molecular clouds is measured to be $\tau_{\rm feedback} = 0.7^{+0.3}_{-0.2}$ Myr for our sample of galaxies. Our measurements suggest that molecular clouds spend $\approx 70\%$ of their time with massive stars embedded for almost all of the galaxies in our sample except M51 (see measured $\tau_{\rm feedback} = 1.8 \pm 0.4$ Myr). Note that the $\tau_{\rm feedback}$ obtained using the 24 μm emission ($\tau_{\rm feedback}$, see Table 4). This is expected as 24 μm is already detected during the heavily obscured phase of star formation, making it visible for a longer duration than Hα, which is only detectable when massive stars have formed and surrounding gas and dust have been partially cleared out. By contrast, in the particular case of M51, we find $\tau_{\rm feedback}$ to be shorter than or comparable within the uncertainty to the feedback timescale obtained using Hα. We suspect that such a potentially unphysical measurement could be due to artifacts in the 24 μm map of M51 introduced by the deconvolution algorithm used to create the high resolution map (Dumas et al. 2011). These artifacts are clearly visible as dark rings around bright peaks in the spiral arms of the galaxy, see Figure 1 and Appendix A1 and may or may not make the interpretation of timescales less accurate as discussed in Section 5.1.

The measured durations between the onset of embedded star formation and molecular cloud disruption ($\tau_{\rm feedback}$) are comparable to the time it takes for the first supernova to explode. This is about 3 Myr for a 9 M$_\odot$ star, and 6.5 Myr when the initial mass function is stochastically sampled for the typical stellar region masses considered here (with almost no dependence on metallicity, Chevance et al. 2020a). The measured short feedback timescales indicate that pre-supernova feedback such as photoionization and stellar winds are mostly responsible for the dispersal of molecular clouds. Our measurements of the feedback timescale (0.7–1.8 Myr) show good agreement with the typical age of star clusters when they stop being associated with their natal GMCs in both in the Milky Way and nearby galaxies (e.g. 1 Myr, Lada & Lada 2003; Whitmore et al. 2014; Hollyhead et al. 2015; Corbelli et al. 2017; Grasha et al. 2019; 2019). This is further discussed in Section 5.2. Radiation magnetohydrodynamic simulations of GMCs by Kim et al. 2020 suggest a similar duration for the star formation and feedback timescales (2–3 Myr). The measured duration of embedded star formation is somewhat shorter than the age spread of star clusters in the LMC (3.5 Myr, measured by Efremov & Elmegreen (1998)). If the scale of the mean radius of SFR tracer peaks (~11.5 pc, Sec. 5.1) is expected to be the actual size of star-forming region necessary to smaller than the size of SFR tracer peak, which is limited by the spatial resolution of our maps, the agreement gets better. If we only consider the age spreads measured among young stellar clusters (1–4 Myr from star clusters with ages of ~ 11 Myr).

5.1.2. Duration of the 24 μm emission phase

Across all galaxies in our sample, we find that the 24 μm emission phase lasts for 8–14 Myr. For M33, we note that our measurement of $\tau_{\rm 24\mu m}$ is very good agreement with the one from Corbelli et al. (2017), where 24 μm emission is found to last for ~10 Myr after the onset of massive star formation by applying a cloud classification method to M33. The ratio between duration of visibility of 24 μm and the feedback timescale ($\tau_{\rm 24\mu m}/\tau_{\rm feedback}$) ranges from 0.8 to 5.3.

The 24 μm emission does not originate only from embedded young massive stars, but also from late-type stars and the interstellar radiation field which make a non-negligible contribution to the dust heating (Draine & Li 2007; Verley et al. 2009). The contribution of the sources not related to recent local massive star formation to the 24 μm emission is more homogeneously spread in the galaxy compared to the more clustered young stellar population (e.g. Dale et al. 2007; Leroy et al. 2012) and results in an additional diffuse component to the 24 μm emission on large scales. We separate the diffuse emission from the compact emission of young stellar regions by applying the filtering process described in Section 4. The fact that in most galaxies the end of the 24 μm emission phase is before or similar to the end of the Hα emission phase (see Figure 3) shows that this procedure effectively removed contamination from stellar populations not related to recent massive star formation (Section 5.3). We discuss in more detail the effects of starless dust clumps illuminated by external radiation and late-type stars that preferentially locate near their birth sites which might not be removed by our filtering process.

We note that while the duration of the isolated Hα emission phase ($\tau_{\rm H\alpha}$) is almost constant in all the galaxies in our sample by construction (Haydon et al. 2020), the duration of isolated 24 μm emission ($\tau_{\rm 24\mu m}$) appears to vary across the sample, ranging from 1.1 Myr (excluding M51) to the end of the Hα emission phase (8.0 Myr). The isolated phase originates from stochastic sampling of small dust clouds. We note that the phase is shorter for star-forming regions in more metal-rich galaxies (see Figure 1 and 4). This is discussed in more detail in Section 5.3.

5.1.3. Region separation length

As visible in Figure 2, gas and SFR tracer peaks are spatially decorrelated on small spatial scales, revealing that galaxies are made of regions that are independently undergoing evolution from molecular gas to stars. The spatial scale at which the gas-to-SFR ratio averages from galactic average (Figure 9) is linked to the typical distance d between independent regions. We find that d ranges from 90 pc to 190 pc for the galaxies in our sample when considering the 24 μm and CO emission maps. For M51, we do not sufficiently resolve the region separation length and are only able to obtain an upper limit (see Section 5.1.1). For the other galaxies we find that derived using 24 μm maps and Hα maps agree within the formal uncertainties.

While the physical mechanism that sets the region separation length remain debated, similarity between the region separation length and the gas disk scale height has been reported by Krumholz et al. 2019 in NGC 300 suggesting that the depressurisation of H II regions along the direction perpendicular to the galactic disk might be responsible for this characteristic length. Furthermore, the measured values of d are comparable to the thickness of the vertical distribution of star-forming regions underground in earlier stages of evolution (150–200 pc) observed using *Spitzer* IRAC 8 μm maps of edge-on spiral galaxies (NGC 891 and IC 5052) (Elmegreen & Elmegreen 2020). If the thickness of the molecular disk measured with CO emission (Scoville et al. 1993; Yim et al. 2014; Heyer & Dame 2015; Patra 2020; Yim et al. 2020), and also to the amplitude of the oscillation seen in the Radcliffe Wave recently discovered in the vicinity of the Sun (Alves et al. 2020), finally the region separation length roughly coincides with the spatial wavelength of velocity corrugations in NGC 4321 (Henshaw et al. 2020) indicating that it matches the scale on which the molecular interstellar medium is reorganised by cloud-scale turbulent flows. Further investigation is needed to verify quantitatively whether the correlation observed by Krumholz et al. 2019 holds more generally in nearby galaxies.

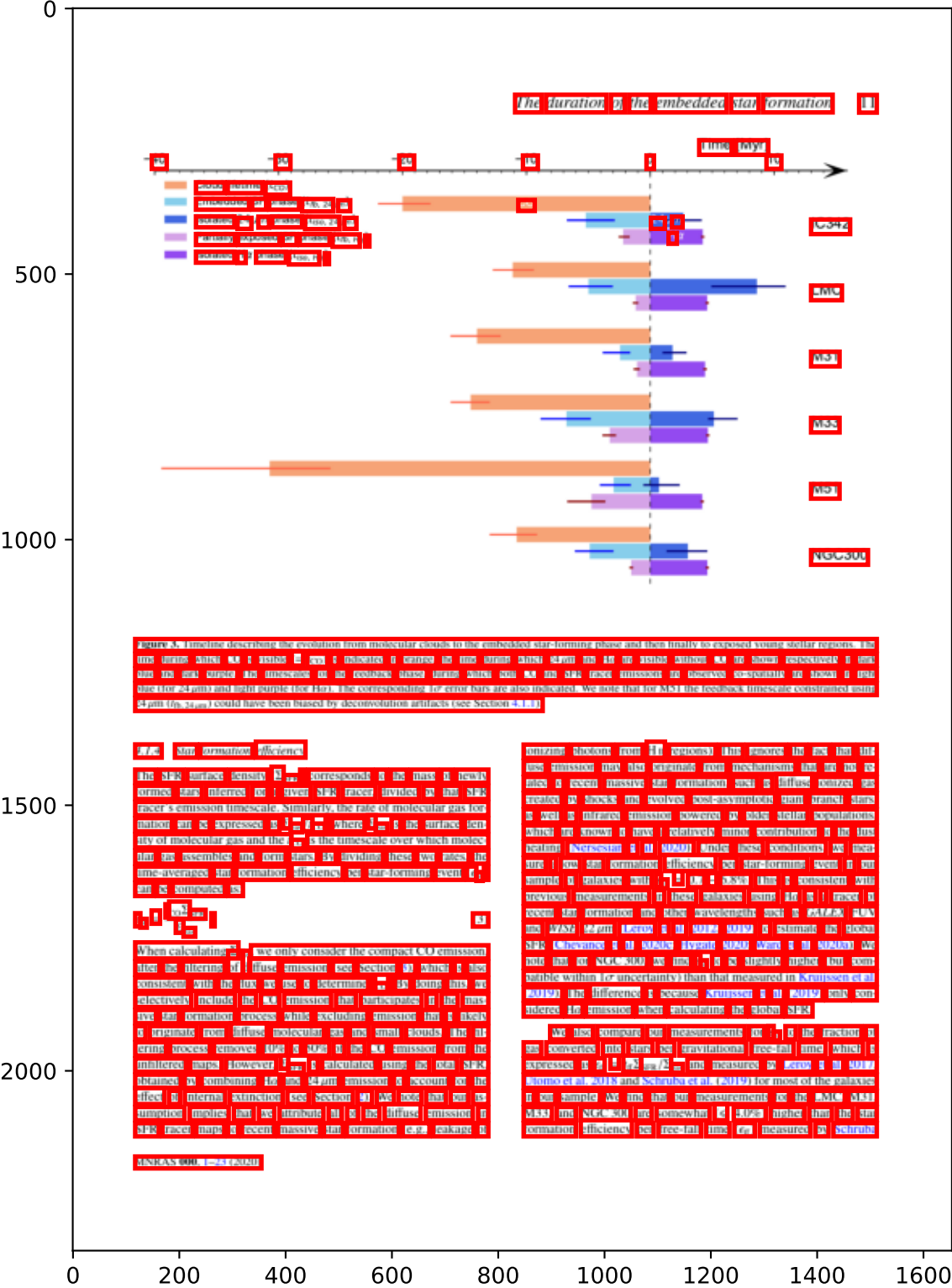

Figure 3. Timeline describing the evolution from molecular clouds to the embedded star-forming phase and then finally to exposed young stellar regions. The time during which $\alpha_{\rm CO}$ is (also) a function of gas is indicated in orange, the time during which 24 μm and/or 8 μm is (also) a function of age in green, and the timescale of the feedback phase during which both $\alpha_{\rm CO}$ and SFR tracer emission are observed co-spatially is shown in light blue (for 24 μm) and light purple (for Hα). The corresponding 1σ error bars are also indicated. We note that for M51 the feedback timescale constrained using 24 μm ($t_{\rm fb,24\,\mu m}$) could have been biased by deconvolution artifacts (see Section 4.1.1).

4.1.4 Star formation efficiency

The SFR surface density $\Sigma_{\rm SFR}$ corresponds to the mass of newly formed stars inferred from a given SFR tracer, divided by that SFR tracer's emission timescale. Similarly, the rate of molecular gas formation can be expressed as $\Sigma_{\rm mol}/\tau_{\rm dep}$, where $\Sigma_{\rm mol}$ is the surface density of molecular gas and the $\tau_{\rm dep}$ is the timescale over which molecular gas assembles into stars. By dividing these two rates, the time-averaged star formation efficiency per star-forming event, $\epsilon_{\rm ff}$, can be computed as:

$$\epsilon_{\rm ff} = \frac{\Sigma_{\rm SFR}}{\Sigma_{\rm mol}/\tau_{\rm dep}} \quad (8)$$

When calculating $\Sigma_{\rm SFR}$, we only consider the compact CO emission after the filtering of diffuse emission (see Section 3.1, which is also consistent with the fluxes used to determine $\alpha_{\rm CO}$). Doing this will effectively include the CO emission that participates in the massive star formation process, while excluding emission that is likely originate from diffuse molecular gas and small clouds. The filtering process removes 10% (5–30%) of the CO emission from the unfiltered maps. However, $\Sigma_{\rm SFR}$ is calculated using the total SFR obtained by combining the raw 24 μm emission to account for the effect of internal extinction (see Section 3.1). We note that this assumption implies that we attribute all of the diffuse emission in SFR tracer maps to recent massive star formation, e.g. leakage of ionizing photons from H II regions. This ignores the fact that diffuse emission may also originate from mechanisms that are not related to recent massive star formation, such as diffuse ionized gas heated by shocks and/or evolved post-asymptotic giant branch stars, as well as infrared emission powered by older stellar populations, which are known to have a relatively minor contribution to the luminosity (Nersesian et al. 2020). Under these conditions, we measure a low star formation efficiency per star-forming event for our sample of galaxies with $\epsilon_{\rm ff} = 0.8\%$, this is consistent with previous measurements of these galaxies using IR as a tracer of recent star formation and other wavelengths such as GALEX FUV and WISE 12 μm (Leroy et al. 2012, 2019) to estimate the global SFR (Chevance et al. 2020a; Hygate et al. 2020; Ward et al. 2020a). We note that for NGC 300, we find $\epsilon_{\rm ff}$ is slightly higher but consistable within 1σ uncertainty) than that measured in Kruijssen et al. (2019). The difference is because Kruijssen et al. (2019) only considered Hα emission when calculating the global SFR.

We also compare our measurements of $\epsilon_{\rm ff}$. The fraction is also converted into star-to-gravitational free-fall time, which is expressed as $t_{\rm ff}/\tau_{\rm dep} = \sqrt{3\pi/32G\rho}/\tau_{\rm dep}$ and measured by Leroy et al. (2017), Utomo et al. (2018) and Schruba et al. (2019) for most of the galaxies in our sample. We find that our measurements for the LMC, M31, M33 and NGC 300 are somewhat (~0.05 dex) higher than the star formation efficiency per free-fall time ($\epsilon_{\rm ff}$) measured by Schruba

S. H. 2019) which are 0.5% 0.7% 0.5% and 1.2% respectively because the cloud lifetime in these galaxies is similar to the free-fall timescale (Schruba et al. 2019) this difference is mostly due to the fact that we measure gas surface density from the diffuse emission filtered out by the map in order to calculate the fraction of compact clouds turning into stars for M51 the difference becomes more significant at 1.3–0.36% (Leroy et al. 2017 Chevance et al. 2018) and is because cloud lifetime is almost five times the free-fall timescale

3.1.3. Feedback velocity

As a result of the energetic feedback from young massive stars CO emission becomes rapidly undetectable after the onset of star formation This is most likely due to a phase and density change in the neighbouring medium through kinetic dispersal, ionization, and photodissociation We combine the timescale over which molecular clouds are disrupted by feedback, t_{fb} with the characteristic size of the clouds detected in CO R_{CO} to define the feedback velocity as $v_{fb} = R_{CO}/t_{fb}$ the size of the cloud is measured from our method by fitting a gaussian profile to the surface density contrast between the peak and the background and ranges between 10–40 pc for our sample of our galaxies This velocity represents the speed of the kinetic removal of molecular gas as the phase transition from depending on the nature of the dispersal mechanism We use zero t_{fb} as define assuming that disruption of the molecular gas starts with the young stellar population becoming partially exposed whereas the 24 μm emission over taking the heavily obscured phase where the expansion of the H II region has not yet begun and during which gas accretion onto the cloud potentially continues This derived v_{fb} ranges between 1 8 km s^{-1} which is comparable to the measurements of expansion velocities in nearby H II regions. For example, the expansion velocities of five H II regions in NGC 300 are measured to be in the range of 5 – 30 km s^{-1} (McLeod et al. 2020) similar values are also found for H II regions in the LMC (Nazé et al. 2001 2002 McLeod et al. 2019) and the Milky Way (Murray & Rahman 2010; Barnes et al. 2020). Numerical simulations of star-forming regions (e.g. Kim et al. 2018) also support this range of values

3.2. Heavily obscured phase of star formation

In order to probe the earliest phase of star formation which is mainly associated with 24 μm emission and not with H II because of strong attenuation provided by the surrounding gas we measure the duration of the heavily obscured phase of star formation as the difference between the feedback timescale and 24 μm emission (or CO for 24 μm emission i.e. the duration of the heavily exposed phase of star formation) $t_{obscured} = t_{24\,\mu m} - t_{fb}$ We omit M33 here because the insufficient resolution of the 24 μm map only allows us the determination of an upper limit of $t_{obscured}$ see section 3.1.1 and the presence of deconvolution artifacts see section 3.1.1 could have biased our measurements especially for timescale-related quantities. However, we retain M51 in our sample of large as shown our unsuccessful attempt of applying the method to 24 μm emission map that has been created using the HiRes de-

[illegible] M51 see figure 3) the measured duration is comparable to our estimates of heavily obscured star cluster in the Milky Way 0.5–3 Myr see Lada & Lada 2003 and references therein A similar duration of the highly embedded star-forming phase has recently been reported by Kimmegreen & Kimmegreen (2019 0200) where such a phase is suggested as an at least 1 Myr based on the mass measurement of star-forming cores in nearby spiral galaxies using 8 μm emission This measurement of 0.5 Myr or the heavily obscured phase using cloud classification method by Corbelli et al. (2017) also supports the values we obtain here see more in section 6.2)

3.3. Relation with environmental properties

We now explore potential environmental dependences of the durations of the successive phases of cloud evolution and star formation In Figure 4 our measurements of the durations of the heavily obscured phase ($t_{obscured}$) the total 24 μm emission phase ($t_{24\,\mu m}$) the isolated 24 μm emission phase ($t_{isolated}$ = $t_{24\,\mu m}$ − t_{fb}) and the feedback phase (t_{fb}) are shown in the top four rows as a function of local cloud-scale and galactic properties such as the mass weighted mean molecular gas surface density (Σ_{GMC}) as measured in Schruba et al. (2021) or (C-34) and Schruba et al. (2019) or the other galaxies) metallicity relative to solar metallicity (Z) integrated star formation efficiency per star formation event (SFE) surface density Σ_{SFR} and the feedback velocity v_{fb} In order to look for correlations with these environmental properties we use LINMIX (Kelly 2007) a Bayesian method for accounting for measurement error in mean regression We fit for any statistically significant trend which is defined as a positive or negative with 95% probability While this is not shown in Figure we also found no statistically significant correlation with the galaxy-averaged molecular gas surface density Σ_{GMC} However we note that $t_{obscured}$ and $t_{isolated}$ appear to be somewhat shorter towards increasing metallicity or and decreasing star formation efficiency While it is difficult to distinguish what is driving the trend in metallicity and star formation efficiency we correlate it to our sample of galaxies we suspect that metallicity could be the primary driver of this trend Indeed winds from massive stars become more energetic with increasing metallicity Maeder (1992) resulting in faster dispersal of the surroundings gas and decay of $t_{obscured}$ emission We note that we might expect a less longer isolated 24 μm emitting timescale for metal rich galaxies since the just-to-gas ratio correlate with metallicity (Remy-Ruyer et al. 2014) that is not what we find here which can be explained by our use of relative change of gas-to-SFR tracer flux ratio compared to the galactic average instead of using absolute flux ratios when constraining the timeline of GMC evolution The relative fractions of $t_{obscured}$ and $t_{isolated}$ compared to t_{fb} are plotted against galactic properties in the bottom two rows of Figure 4 We again see no anticorrelation of these durations with metallicity and a correlation with star formation efficiency, while no statistically significant trend is found with respect to galactic properties using the same regression analysis (Kelly 2007) Our result (bottom row) show that clouds in the LMC M33 and NGC 300 spend a larger fraction of their lifetime with embedded massive star formation ~40% compared to clouds in C-34 and M51 ~20% with an average of 46% across our sample of galaxies

[illegible] the total mass contained in molecular clouds. Including these clouds would not change our conclusion

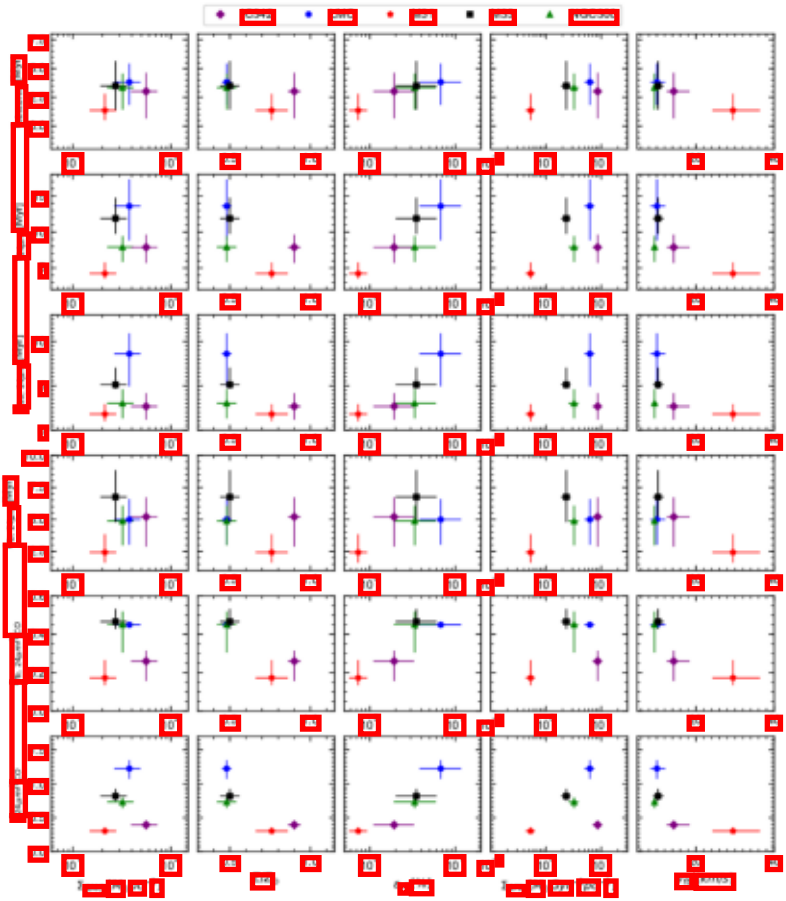

Figure 4. In the top four rows, our measurements of the duration of the heavily obscured phase ($t_{\rm obscured} = t_{\rm fb,24\,\mu m} - t_{\rm fb,8\,\mu m}$), the 24 μm emitting phase ($t_{24\,\mu m}$), the isolated 24 μm emitting phase ($t_{\rm iso,24\,\mu m} = t_{24\,\mu m} - t_{\rm fb,24\,\mu m}$), and the feedback phase ($t_{\rm fb,24\,\mu m}$) are shown as a function of galactic (or cloud-scale) properties, i.e. the mass-weighted mean molecular gas surface density of GMCs ($\Sigma_{\rm GMC}$) measured in Schruba et al. (2019) and Schruba et al. (2021a), metallicity ($Z/Z_\odot$), star formation efficiency ($\epsilon_{\rm ff}$), SFR surface density ($\Sigma_{\rm SFR}$) and the feedback velocity ($v_{\rm fb}$). The bottom two rows show the ratios of the feedback timescale and the 24 μm emitting phase to the cloud lifetime ($t_{\rm fb,24\,\mu m}/t_{\rm CL}$ and $t_{24\,\mu m}/t_{\rm CL}$), as a function of the same galactic properties.

5 DISCUSSION

5.1 Robustness of the results

5.1.1 Satisfaction of guidelines of Kruijssen & Longmore (2014)

We verify here that our analysis satisfies the requirements listed in Section 3.2 of Kruijssen & Longmore (2014). Satisfaction of these criteria indicates that the constrained parameters ($t_{\rm obscured}$, $t_{24\,\mu m}$, $t_{\rm iso,24\,\mu m}$, and $t_{\rm fb,24\,\mu m}$) are measured with the accuracy of a gas-PDF-based analysis as the fraction of SFR tracer we can check the accuracy of $t_{\rm obscured}$ and $t_{24\,\mu m}$ because the measurements for other galaxies have not yet been validated by previous studies (see Kruijssen & Longmore 2014, Chevance et al. 2020, Hygate et al. 2020, Ward et al. 2020a).

1. The duration of an extra stellar phase should always differ less than one order of magnitude. This condition is satisfied as

log $\left(\frac{\Sigma_{\rm SFR}}{\Sigma_{\rm H_2}}\right)$ 0.5 in C 342, the M51, the log $\left(\frac{\Sigma_{\rm SFR}}{\Sigma_{\rm H_2}}\right)$ 0.92 or 0.1 in galaxies in our sample where the difference between $\Sigma_{\rm SFR}$ and $\Sigma_{\rm H_2}$ is larger in M51 while those in other galaxies are log $\left(\frac{\Sigma_{\rm SFR}}{\Sigma_{\rm H_2}}\right)$ 0.52.

In fact, for almost all of the galaxies except M51, we measure $\Sigma_{\rm H_2}$ > $\Sigma_{\rm SFR}$ which ensures that the region separation length is sufficiently resolved by our observations. For M51, we measure $\Sigma_{\rm H_2}$ < $\Sigma_{\rm SFR}$ implying that $\Sigma_{\rm SFR}$ can be constrained with sufficient accuracy only in the upper limit case as derived as in Section 3.2.2.

iii) The number of detached emission peaks is always above 20 with in the 3.8 arcsec 24 μm emission maps, as well as in the maps of C 342 and M51.

iv) The measured gas-to-SFR mix ratios occasionally at low SFR tracer peaks should never be below above the galactic average. This condition may not always be true if the presence of diffuse emission reservoir is visible in figure 9 but interior satisfies this, we infer in its large-scale diffuse emission of both tracer maps.

v) In order to perform accurate measurements, we require the global star formation history to not vary more than 0.1 dex during the duration of the whole evolutionary cycle, ranging from ≈ 15 to 35 Myr, of our sample when averaged over time intervals of width $\Delta t_{\rm avg}$ = 3 Myr. Using multi-wavelength data of the LMC and synthetic stellar population models, Harris & Zaritsky (2009) studied the star formation history of the LMC and found a roughly consistent SFR during the duration of the whole evolutionary cycle. The interior satisfies of M33 and NGC 300 is shown by Kang et al. (2012, 2016) using chemical evolution models to reconstruct the star formation rate history. Using data from the PHAT survey, the recent star formation history of M31 is confirmed to be quiescent without significant variations (Lewis et al. 2015; Williams et al. 2017) by performing spectral energy distribution fitting of the multi-wavelength data of M31 for SFR of M31 is also measured to be roughly constant for the last 100 Myr (Lufrasio et al. 2017). The star formation history of C 342 is not known. However, we do not expect it to experience significant variations of the global star formation rate during the last 5-30 Myr when averaged over $\Delta t_{\rm avg}$ = 3 Myr. In addition, we mask the starburst nucleus of this galaxy, which experienced a major burst of star formation 60 Myr ago (Boker et al. 1999).

vi) Each independent region should be detectable if even low activity in both tracers at some point in their life. In order to check this condition, satisfied for our sample of galaxies, we first calculate the minimum star-forming region mass expected to form from the detected molecular clouds by multiplying the star formation efficiency obtained in our method, see table 3, by the 3σ point source sensitivity limit in the 3.8 arcsec map. We then compare this mass to the mass of the stellar population required to provide the ionizing radiation luminosity that matches the 3σ sensitivities of 24 μm and Hα maps on the scale of individual star-forming regions. (1) We use the Starburst99 model (Leitherer et al. 1999) to calculate the initial mass of the stellar population assuming stars formed instantaneously 5 Myr ago (similarly to the Hα emitting timescale). Since Starburst99 only provides models of the Hα luminosity as a function of the age of the stellar population of different metallicities, we use the relation from Kennicutt & Evans (2012) and references herein), $\log(\Sigma_{\rm SFR}$ [$M_\odot$ yr^{-1} kpc^{-2}]$) = -41.27 + \log(\nu I_{\nu}$ [erg s^{-1} cm^{-2}]$) - 42.69$, to obtain a similar estimator of the 24 μm luminosity. We find that the minimum mass of the stellar population obtained from 3σ maps agrees well with that obtained from 24 μm and Hα maps ranging from 10^4 to 7.5 × 10^4 $M_\odot$ for the galaxies of our sample. This testing has the sensitivity of the 24 μm SFR tracer maps are well matched and the faintest CO peak is likely to evolve into the faintest Hα region. In principle, clouds can disperse dynamically before forming massive stars and their assembling of this case be time spent before GMC dispersal would be added by our method of the measured lifetime of clouds that do form massive stars. However, Kruijssen & Longmore (2019) and Chevance et al. (2020c) show that this is unlikely to happen because the clouds are found to live only for about the dynamical timescale not leaving enough time for cloud dispersal and recollapse before forming massive stars.

Most of our measurements of $\Sigma_{\rm SFR}$ and $\Sigma_{\rm H_2}$ of the galaxies in our sample as well as the $\Sigma_{\rm SFR}$ and $\Sigma_{\rm H_2}$ of C 342 and M31 will be of SFR tracer are validated by satisfying the conditions listed above. The only exceptions are of M51 where we neither have sufficient resolution to accurately constrain the region separation length for the feedback timescale. Only upper limits can be obtained for these values in order to determine whether our measurements are reliable or not. For all the galaxies in our sample and $\Sigma_{\rm SFR}$ of C 342 and M31 we use four additional criteria listed in Kruijssen & Longmore (2018) to do so. We introduce the clump factor of SFR tracer to tracer peaks as $f = \left(\frac{N_{\rm peak}}{N_{\rm tot}}\right)$ where $N_{\rm peak}$ is the mean radius of the corresponding peaks. This parameter characterises how densely the peaks are distributed in a map.

vii) If peaks are densely distributed and potentially overlapping with each other, the density contrast used for peak identification $\log(\alpha)$ should be small enough to identify adjacent peaks. We compare the figure 6 scan values to $\log(\alpha)$ with the upper limit prescribed by Kruijssen et al. (2018) and show that our choice stability for appropriate detection of neighbouring peaks even in densely populated environments.

viii) For an accurate measurement of the feedback timescale contamination by neighboring peaks should be small enough to feed a spatial overlap of neighbouring peaks due to low resolution or blending can be caused attributes a clump temporal overlap therefore artificially increasing the duration of the measured feedback timescale. If this case, only an upper limit of the feedback timescale can be determined. In figure 9, we compare the analytical prescription of Kruijssen et al. (2018) with our measurements of $\Delta t_{\rm SF}$ as average of where $\Delta t_{\rm SF}$ is the total duration of the whole evolutionary cycle ($\Delta t_{\rm SF} = \frac{1}{\Sigma_{\rm SFR}} \int_{\Sigma_{\rm SFR}=0}^{\Sigma_{\rm SFR}=\Sigma_{\rm SFR}(t)} d\Sigma_{\rm SFR}$). The averaged values are weighting the clump factor of the SFR tracer peaks by their corresponding timescales. We find that this condition is not satisfied for $\Sigma_{\rm SFR}$ of M51. Only upper limits can be determined, see table 3.

ix) Figure 9 shows that the conditions $\Delta t_{\rm SF}$ ≤ 0.1 Gyr and $\Delta t_{\rm SF}$ ≤ 1.5 Gyr are verified for all galaxies.

x) Similarly to condition vi) the SFR should not vary more than 0.1 dex during the entire timeline when averaged over the width of feedback timescale. This condition is also satisfied using the same reasoning as states in v) above.

xi) After masking obvious stellar regions such as galactic centres, visual inspection of the maps does not reveal abundant blending. Figure 10.

Overall we find that our measurements are reliable except for Hα and $\Sigma_{\rm SFR}$ of M51. These two measurements should formally be considered as upper limits as they do not satisfy conditions iii, viii). However, we note that the deconvolution artifact present in the 24 μm map of M51 may or may not affect the feedback timescale and therefore the value we obtain is its upper limit should be considered uncertain.

5.1.2 Effect of spatial resolution and inclination on the measurements

In order to test the potential effect of spatial resolution on our measurements we have degraded the resolution of the 8 μm emission maps of NGC 300 to the coarsest resolution (100 pc) of galaxy sample 1 (see Table 1) and repeated the analysis described in Section 3. We choose NGC 300 for this test as it does not require much star-forming regions to be masked like in the LMC and M33, making an application of the method more straightforward. We find that timescales of $\tau_{\rm dep}$ = 3.4$^{+0.6}_{-0.5}$ Myr, $\tau_{\rm sf}$ = 1.8$^{+0.3}_{-0.3}$ Myr and the mean separation length of d = 31$^{+2.5}_{-2.5}$ pc are measured at a different spatial resolution are consistent within the uncertainties with the results of Table 9 confirming previous resolution tests on simulated galaxies (Kruijssen et al. 2018) and on NGC 300 (Kruijssen et al. 2019) using the 8 μm SFR tracer.

We have also examined the possible effect of inclination of our measurements by repeating the analysis on CO and 24 μm emission maps of NGC 300 which have been artificially inclined under the assumption of the highest inclination angle among our galaxy sample, M33 (i = 56.0°). We find that measured timescales of $\tau_{\rm dep}$ = 10.4$^{+0.8}_{-0.8}$ Myr, $\tau_{\rm sf}$ = 1.9$^{+0.3}_{-0.3}$ Myr and the mean separation length of d = 92$^{+7.5}_{-7.5}$ pc agree within the uncertainties with those of NGC 300 from Table 9. This is already expected from simulations performed by Kruijssen et al. (2018) using simulated galaxies, where our method has been shown to provide reliable measurements even for a highly inclined galaxy as long as independent star-forming regions are sufficiently resolved ($d > 2\,\sigma_{\rm res}$, see discussion in Section 5.1.1).

5.2 Comparison with other works

The duration of the embedded star-forming phase has been measured in M33 by Corbelli et al. (2017) using IRAM CO data and the mid-infrared source catalog created by Sharma et al. (2011). These work classifies star-forming regions into different evolutionary stages based on the presence of 8 μm emission, the SFR tracer, and 24 μm and Hα or 8 μm emission. The clouds are defined as in an inactive stage when no sign of star formation is detected in embedded star-forming phase when 8 μm emission is observed in association with 24 μm but without associated Hα or FUV emission. The region is defined to be at an exposed star-forming phase when Hα or FUV emission becomes visible.

The age estimates of the exposed star-forming regions referred as B-type in Corbelli et al. (2017) from spectral energy distribution (SED) fitting are available in Sharma et al. (2011) and are obtained using photometric data in various wavelengths simultaneously, such as UV, Hα and 24 μm. The age of the C-type phase corresponds to the time taken for the cloud to evolve from the end of the heavily obscured phase to star formation observed with 8 μm but without Hα or the end of the exposed young stellar object phase (both 8 μm and Hα are observed). The duration therefore corresponds to $\tau_{\rm sf}$ + $\tau_{\rm exposed}$ in our analysis. Corbelli et al. (2017) find that the C-type phase in M33 last for 1.5 Myr without quoted uncertainty, which is in excellent agreement with our measurement of 1.8$^{+0.3}_{-0.3}$ Myr for the duration of the heavily obscured phase of star formation (CO and 24 μm emission without Hα) referred as C-type in Corbelli et al. (2017) and 1.9 Myr which is similar to the duration we measure not only for M33, 3.5$^{+0.6}_{-0.5}$ Myr, but for most of the galaxies of our sample, 1.4 – 1.8 Myr, see Section 5.2.1. Lastly, for the duration of the inactive phase, referred as A-type, we measure $\tau_{\rm dep}$ − $\tau_{\rm sf}$ = 7.7$^{+0.8}_{-0.8}$ Myr which is

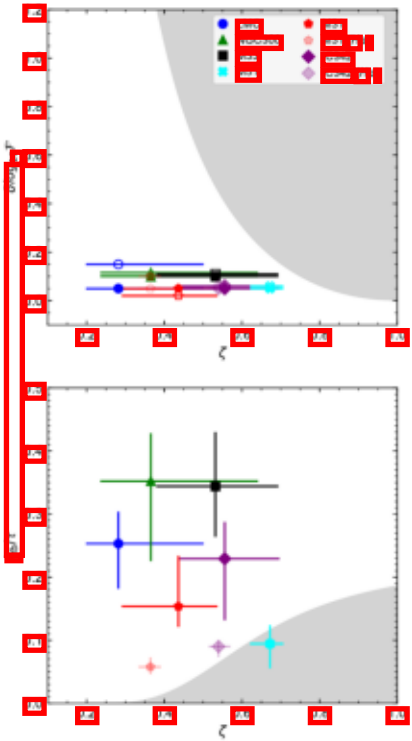

Figure 5. Effects of blending on the feedback timescale measurements. The top panel shows the adopted density contrasts ($\delta\log(\Sigma_{\rm gas})$) used for peak identification of each 24 μm filled symbols and 8 μm open symbols emission maps as a function of the average filling factor of the transparent marker on the x-axis and the y-axis indicates the adopted $\delta\log(\Sigma_{\rm gas})$ for measurements of the analysis with Hα as SFR tracer. The shaded area indicates the region of the parameter space where peak identification is affected by blending (Kruijssen et al. 2018). Our results are well outside of the shaded area, confirming that we adopt small enough $\delta\log(\Sigma_{\rm gas})$ to identify adjacent peaks even in maps with high filling factor. The bottom panel shows the ratio between the feedback timescale ($\tau_{\rm fb}$) and the star formation timescale ($\tau_{\rm sf}$) as a function of the average filling factor. The grey shaded area indicates the region of the parameter space where the contamination by neighbouring peaks affects the measurement of the feedback time scale, resulting only in upper limits. Arrows indicate the $\tau_{\rm fb,\,3\,Myr}$ of M33, where accurate measurements can be made for all other galaxies.

somewhat longer than the measurement in 5 Myr from Corbelli et al. (2017). However, given the uncertainties in age estimates using SED fitting on the order of 0.1 dex and the absence of any uncertainties on their estimates, the evolutionary timeline of molecular clouds in M33 from Corbelli et al. (2017) and our analysis are in good agreement.

The time it takes for star-forming regions to become exposed has also been measured using wavelengths other than 24 μm as a tracer of the embedded star formation. Calzetti et al. (2015) have measured ages of young massive star clusters in the Dwarf Starburst Galaxy NGC 5253 by applying SED modeling techniques to UV-optical-near infrared *Hubble Space Telescope* photometry. While the star clusters have ages spanning from 1 Myr to 8 Myr, the age estimate in one very heavily obscured cluster with a weak near-infrared excess indicates that the duration of the heavily obscured phase of star formation is longer than or similar to 4 Myr in this particular star-forming region. Whitmore et al. (2014) used free-free radio continuum emission to detect heavily obscured star forming regions in the starburst/merger evolutionary timeline from quiescent molecular clouds to exposed star-forming clusters using age estimates from SED fitting of young stellar regions in the overlapping region of the merging Antennae galaxies. The duration of the heavily obscured phase referred to as Stage 1 in Whitmore et al. (2014) and the feedback timescale including the embedded phase referred to as Stage 1 in Whitmore et al. (2014) are measured to be 0.1 – 1 Myr and 2 – 3 Myr, somewhat shorter than the duration we measure with 24 μm, which are 1.8 ± 0.3 Myr and 3.1 ± 0.3 Myr, respectively. We note that the difference could be because of the measurements are for galaxies undergoing a merger, unlike our sample of 12 different galaxies. Dust and gas embedded star formation and their age estimates in highly extinctied regions have considerable uncertainties (Hollyhead et al. 2015).

In conclusion, despite differences in methods, wavelengths and galaxies used, when constraining the evolutionary cycle of star forming regions, our results are in good agreement with the measured timescales for the heavily obscured phase and feedback phase found in previous literature. The key step made in the present work is to generalise these results to a sample of nine galaxies exposed (M51) analysed homogeneously with a single analysis framework that is agnostic about which entities constitute a GMC or star forming region.

5.3 Effects of infrared emission not associated with local recent massive star formation

24 μm emission is widely used as a tracer of embedded star formation, as it captures emission of massive stars that has been reprocessed by dust grains see e.g. Calzetti et al. (2007), Kennicutt & Evans (2012), Yuksalchayabi & Evans (2015). However, one of the known issues with using 24 μm emission as a trace recent star formation is that the interstellar radiation field, late-type stars, age of < 100 Myr) and dust clumps heated by external radiation each is nearby star-forming regions also contribute to the emission at this wavelength (Calzetti et al. (2007), Murphy et al. (2011), Kennicutt & Evans (2012), Leroy et al. (2012).

This difference of a priori distributions associated with each process generating 24 μm emission allows us to separate the emission for recent star formation events from other sources. The 24 μm emission originating from the interstellar radiation field has an extended morphology because it originates from small dust grains in the diffuse interstellar medium (Draine & Li (2007), Draine et al. (2007), Leroy et al. (2009), Kahanamoku et al. (2013), Leroy et al. (2012).

Such diffuse emission, constituting on average of 55% of the 24 μm emission, is therefore expected to be removed during our filtering process.

On the other hand, the effect of 24 μm emission associated with late-type stars and starless dust clumps might not be filtered out because they are more inhomogeneously distributed similarly to the emission from young star-forming regions. To estimate the effect of late-type stars and externally illuminated dust clumps in our measurements, we make use of the far-infrared source catalogue of the LMC, provided by Seale et al. (2014). In this catalogue, young stellar objects and dust clumps (that may or may not have deeply embedded young stars) are identified as well as sources not related to recent star formation such as asymptotic giant branch stars, planetary nebulae, and supernova remnants (using literature catalogs Seale et al. 2014 and references herein). In order to test whether the inclusion of 24 μm emission from older stars and dust clumps could bias our results, we mask these sources and repeat our analysis as the LMC. When masking dust clumps, we mask all the probable candidates in Seale et al. (2014). It is difficult to distinguish whether these clumps harbour deeply embedded stars or are heated by external radiation. We find that the older stars and dust clumps have a negligible effect on our results in practice, under stars and dust clumps are not usually identified as SFR tracer peaks in our analysis due to their low brightness and small size which does not satisfy the requirement of a minimum number of pixels to be identified as a peak in our method.

In conclusion, once the diffuse emission has been filtered in 24 μm maps, mostly contain emission from young stars. Any potential bias due to interstellar radiation field, late-type stars and dust clumps is negligible in our measurements. This provides an accurate characterisation of the duration of partially embedded massive stars.

7 CONCLUSION

We present a characterisation of the evolutionary timeline from molecular clouds to young stellar regions in six nearby galaxies by applying the statistical method developed by Kruijssen & Longmore (2014) and Kruijssen et al. (2018) to CO and 24 μm emission maps at cloud-scale (20–100 pc) resolution. With this method, we measure the duration of the 24 μm emission phase (τ_{24}) in the catalogs, the feedback phase ($\tau_{feedback}$), during which massive star formation continues embedded in molecular clouds, the duration of the heavily obscured star formation phase with no associated H II emission ($\tau_{obscured}$), and the average distance between independent star-forming regions evolving from clouds to massive star formation (λ). We also derive other physical quantities such as the feedback velocity (v_{fb}), the integrated star formation efficiency per star formation event (ϵ_{ff}) from our measurements.

Across our sample of galaxies, we find that molecular clouds are quickly disrupted within 5 – 6 Myr after the onset of embedded massive star formation traced by 24 μm emission by stellar feedback, supporting the idea that GMCs are dispersed within a cloud dynamical timescale, as suggested by Elmegreen (2000) and Hartmann (2001). The measured feedback timescale, which includes the duration of the massive star-forming phase, constitutes 17–47% of the cloud lifetime (3.4 ± 0.9 Myr). The feedback timescales are generally shorter than the time it takes for the first supernova to explode (6 ± 3 Myr) when stochasticity of the initial mass function is taken into account (Chevance et al. 2020). This suggests that early feedback mechanisms such as photoionization and stellar winds are

mainly responsible for the dispersal of molecular clouds. Previous works have found similar duration of this phase using age estimates of star clusters in the Milky Way and some nearby galaxies (Leitner & Lada 2003; Whitmore et al. 2014; Corbelli et al. 2017). After the molecular gas is dispersed, the 24 μm emission decays within 3.0 ± 0.5 Myr. Our results further support the conclusion of earlier work that galaxies are composed of independent star-forming regions separated by ≳ 100 − 200 pc (Kruijssen et al. 2019; Chevance et al. 2020b), which may correspond to the vertical gas disc scale height (see Kruijssen et al. 2019). These regions are underpinned by inefficient star-forming process with integrated cloud-scale star formation efficiencies of ϵ_ff ≈ 0.1% − 0.8%. The measured star formation efficiencies are consistent with previous measurements in these galaxies, along other tracers, estimate the global SFR. We obtain feedback velocities of v_fb ≈ 8 − 31 km s^−1, which is consistent with the observed expansion velocities in nearby H II regions (e.g. Murray & Rahman 2010; McLeod et al. 2019; 2020; Barnes et al. 2020).

By combining our measurements with those using Hα as a tracer, we explore star-forming regions as a function of the evolution of the heavily obscured phase (detected with ALMA and 24 μm but without Hα emission). Our results show that this period lasts for 1.0 ± 0.3 Myr, with a range of 0.4 − 3.8 Myr across our sample of galaxies. We do not detect any significant correlation of the duration of the heavily obscured phase with galactic properties (the measured duration is in good agreement with values suggested in previous works using different wavelengths, methods, and galaxies).

Furthermore, we study the correlation of our measurements with galactic or cloud-scale properties such as mass-weighted mean surface density of CMCs, metallicity, star formation efficiency, SFR surface density, and the feedback velocity. While we do not find statistically significant trends, the durations of the total and isolated 24 μm emission phases (t_24μm and t_24μm,iso) may weakly decrease with increasing metallicity. We conjecture that this dependence results from winds of massive stars being stronger and more energetic at higher metallicities, which leads to a more effective dispersal of the clouds. No such trends with metallicity are observed for the feedback timescale and the duration of the heavily obscured phase.

In order to gain a better understanding of the mechanisms driving the early feedback process, systematic measurements of the embedded phase of a large number of galaxies of various environments is essential. Due to the limited resolution of *Spitzer* 24 μm observations (6.4″), we have been able to perform this analysis for only six nearby galaxies. We accurately constrain the duration of the embedded phase for five of them. In the future, the MIRI imager aboard the *James Webb Space Telescope* will provide a view of 1″×2″, will reach an angular resolution of 0.7″. This will enable the application of the same method to galaxies located out to 15 Mpc covering a much wider range of galaxy properties and morphologies, allowing us to explore how the feedback processes covern the evolution of molecular clouds during the early stages of star formation as a function of the galactic environment.

ACKNOWLEDGEMENTS

We thank an anonymous referee for helpful comments that improved the quality of the manuscript. We thank Alexander Ji for useful suggestions and A. Herrmann for candid chat. US acknowledge funding from the German Research Foundation (DFG) through the DFG Sachbeihilfe grant number KR4801/2-1. MC and MDR gratefully acknowledge funding from the DFG through an Emmy Noether grant (grant number KR4801/1-1). MDR gratefully acknowledges funding from the European Research Council (ERC) under the European Union's Horizon 2020 research and innovation programme via the ERC Starting grant MUSTANG (grant agreement number 714907). MDR gratefully acknowledges funding from the Sonderforschungsbereich SFB 881 (Project-ID 138713538) "The Milky Way System" (subproject A1) of the DFG. FE and ATE would like to acknowledge funding from the European Research Council (ERC) under the European Union's Horizon 2020 research and innovation programme (grant agreement No. 726384/Empire). SCOC thanks the DFG for the collaborative Research Center SFB 881 (Project-ID 138713538) "The Milky Way System" (sub-projects A1, B1, B2 and B8) and from the Heidelberg Cluster of Excellence (EXC 2181 - 390900948) "STRUCTURES: A unifying approach to emergent phenomena in the physical world, mathematics, and complex data" funded by the German Excellence Strategy. They also thank for funding from the European Research Council in the ERC Synergy Grant "ECOSTAR" ("understanding our galactic ecosystem: from the disk of the Milky Way to the formation site of stars and planets", project-ID 855130). KB gratefully acknowledges funding from the German Research Foundation (DFG) in the form of an Emmy Noether Research Group grant (number KR4598/2-1). P. Kreckel thanks Wolf Dietrich Vogt and Kai Sandstrom for partially supported by the National Science Foundation (NSF) under grant Nos. 1615105, 1615109, and 1653300. MQ acknowledges support from the research project PID2019-106027GA-C44 from the Spanish Ministerio de Ciencia e Innovacion. ES thanks IGW acknowledges funding from the European Research Council (ERC) under the European Union's Horizon 2020 research and innovation programme (grant agreement No. 694343). This work was carried out in part in the PHANGS collaboration. This paper makes use of the following ALMA data: ADS/JAO.ALMA#2013.1.00551.S, ADS/JAO.ALMA#2015.1.00258.S. ALMA is a partnership of ESO (representing its member states), NSF (USA) and NINS (Japan) together with NRC (Canada), NSC and ASIAA (Taiwan) and KASI (Republic of Korea), in cooperation with the Republic of Chile. The Joint ALMA Observatory is operated by ESO, AUI/NRAO and NAOJ. The National Radio Astronomy Observatory is a facility of the National Science Foundation operated under cooperative agreement by Associated Universities, Inc. This work makes use of the PDR Arcsecond Survey (Pety et al. 2013; Schinnerer et al. 2013). The authors thank IRAM for making the data products of C-34.2 (Schruba et al. 2021a) M33 (Schruba et al. 2021b) and M33 CO Large Program (Gratier et al. 2010; Druard et al. 2014) available. IRAM is supported by INSU/CNRS (France), MPG (Germany) and IGN (Spain). We thank the IRAM staff for their assistance with the observations.

DATA AVAILABILITY

The data underlying this article will be shared on reasonable requests to the corresponding author.

REFERENCES

Alves J., et al., 2020, Nature, 578, 237
Amaro-Seoane P., Brunt S. N., Gordon K. D., Sandstrom K., 2011, PASP, 123, 1412

Aigrain S., Gibson N., Saunal A. J., Scott P., 2009, MNRAS, 47, 481
Aguilar M., Marscimak R., Barnitty P., 2011, AJ, 142, 137
Backus C., Velusamy T., Thompson R., Arbuzov A., 2005, Hres, super resolution for the Spitzer Space Telescope, p. 0.
Barnes S. I., Longmore S. N., Leis J., Krumholz M. R., Kruijssen J. M. D., Bigiel F., 2020, MNRAS, 498, 4906
Bigiel F., Leroy A., Walter F., Brinks E., Blok W. J. G., Madore B., Thornley M. D., 2008, AJ, 136, 2846
Bilir S., Ishiki S., Kawamura A., Ferro A., Chizuka N., Kosolowsky E., 2007, Astrophys. Lett. Lett. Astrophys. Astron. Astrophys. Astron. Astrophys. Astron

Stetter, R., Weninger, A., Huelsz, M., Ungerechts, H., Lucas, R., Berkhuijsen, E. M., Beck, R., Wielebinski, R., 2006, A&A, 455, 499
Brodera S., et al., 2010, ApJ, 722, 1122
Tafra N. N., 2020, A&A, 638, A64
Tature, J., Beureut, D., Jolliffe, I. T., Longuetheau, J., Coudreau-Durab, N., Hallet, N., Petit, C., 2003a, A&A, 412, 57
Tature, J., Beureut, D., Jolliffe, I. T., Longuetheau, J., Coudreau-Durab, N., Hallet, N., Petit, C., 2003b, A&A, 412, 57
Tety J., et al., 2015, ApJ, 779, 43
Tetrzyński G., et al., 2019, Nature, 567, 210
Tlyagin L. S., 2001, A&A, 369, 599
Tlyagin L. S., Grebel E. K., Mattsson L., 2012, MNRAS, 424, 2310
Tlyagin L. S., Grebel E. K., Zhukovskaya T. A., Khrapov A. A., 2014, AJ, 148, 84
Trescott M. K. M., et al., 2007, ApJ, 668, 18
Turegata M., et al., 2019, A&A, 625, A18
Tahman N., et al., 2011, ApJ, 730, 18
Temy-Rayer A., et al., 2014, A&A, 563, A31
Tieke G. H., et al., 2004, ApJS, 154, 25
Schmeiser E., et al., 2013, ApJ, 779, 45
Schmeiser E., et al., 2019, ApJ, 887, 49
Schlafly E. F., Finkbeiner D. P., 2011, ApJ, 737, 103
Schlegel D. J., Finkbeiner D. P., Davis M., 1998, ApJ, 500, 525
Schmidt M., 1959, ApJ, 129, 243
Schruba A., Leroy A. K., Walter F., Sandstrom K., Rosolowsky E., 2010, ApJ, 722, 1699
Schruba A., Kruijssen J. M. D., Leroy A. K., 2019, ApJ, 883, 2
Schruba A., et al., 2021a, ApJ to be submitted
Schruba A., Leroy A. K., Kepley A. A., Anderson J. P., Sandstrom K., Mac Low, M.-M., Henshaw J. D., Scoville N., Walter F., Weiss D. R., 2021b, ApJ to be submitted
Schuster K. F., et al., 2004, A&A, 423, 1171
Scoville N. Z., Hildebrand R. H., Stratton J. M., Sargent A. I., 1993, ApJ, 404, 92
Seale J. P., et al., 2014, AJ, 148, 124
Sharma S., Corbelli E., Giovanardi C., Hunt L. K., Palla F., 2011, A&A, 534, A98
Sick J., Courteau S., Cuillandre J.-C., Dalcanton J., Dey A., McDonald M., Simard L., Tully R. B., 2015, in Appellari M., Courteau S., eds, IAU Xvi: Galaxy Masses as Constraints of Formation Models, pp 82–88, arXiv:1410.9917, doi:10.1017/S1743921315003440
Silk J., 1997, ApJ, 481, 703
Skibba R. A., et al., 2012, ApJ, 761, 43
Slavelev-Smith L., Kim S., Calabretta M. R., Haynes R. F., Kesteven M. J., 2003, MNRAS, 339, 8
Sorribo San Cipriano L., Garcia-Rojas J., Esteban C., Bresolin F., Peimbert M., 2016, MNRAS, 458, 1869
Sorribo San Cipriano L., Domínguez-Guzmán G., Esteban C., García-Rojas J., Mesa-Delgado A., Bresolin F., Rodríguez M., Simón-Díaz S., 2017, MNRAS, 467, 3729
Homo D., et al., 2018, ApJ, 861, L18
Sorley S., Corbelli E., Giovanardi C., Hunt L. K., 2009, A&A, 493, 453
Stanne S., et al., 2017, A&A, 599, A64
Satisachavakul N., Evans Neal J. I., 2013, ApJ, 765, 128
Ward J. L., Chevance M., Kruijssen J. M. D., Kim J.-G., Hygate A. P. S., Schruba A., Longmore S. N., 2020a, MNRAS to be submitted
Ward J. L., Chevance M., Kruijssen J. M. D., Hygate A. P. S., Schruba A., Longmore S. N., 2020b, MNRAS, 497, 2280
Westmeier T., Braun R., Koribalski B. S., 2011, MNRAS, 410, 2217
Whitmore B. C., et al., 2014, ApJ, 795, 156
Williams J. P., de Geus E. J., Blitz L., 1994, ApJ, 428, 693
Williams B. F., et al., 2017, ApJ, 846, 143
Williams T. G., Gear W. K., Smith M. W. L., 2018, MNRAS, 479, 297
Williams T. G., Baes M., Cooray T., Relaño M., Smith M. W. L., Verstocken S., Viaene S., 2019, MNRAS, 487, 2755
Wong T., et al., 2011, ApJS, 197, 10
Wong T., et al., 2017, ApJ, 850, 139
Wood K., Hill A. S., Joung M. R., Mac Low, M.-M., Benjamin R. A., Haffner L. M., Reynolds R. J., Madsen G. J., 2010, ApJ, 721, 1397

Xu C. K., Lutz D., Braine J., Zhao Y., Cao C., Xiaohong Z., Tacconi L. J., Genzel R., Daddi E., Dannerbauer H., Elbaz D., Gao Y., Gracia-Carpio J., Sanders D. B., Shu X. W., Wang T., Wang W. H., Wang Z., Wu H., Yan L., Zhong J., Zhu M., 2012, ApJ, 752, 603
Yun K., Wong T., Kim S., Kim J.-H., Rosolowsky E., Lin W., Hughes A., Gallagher III J. S., Benjamin R., Murphy E. J., 2014, AJ, 148, 123
Yun K., Wong T., Kauffmann E., 2020, MNRAS, 499, 4200
Zabel N., et al., 2020, MNRAS, 496, 2123
Zurita A., Bresolin F., 2012, MNRAS, 427, 1463
da Silva R. L., Fumagalli M., Krumholz M., 2012, ApJ, 745, 145
da Silva R. L., Fumagalli M., Krumholz M. R., 2014, MNRAS, 444, 3275

APPENDIX A: INDIVIDUAL IMAGES OF EMISSION MAPS USED IN OUR ANALYSIS

In Figures A1 and A2, we present the CO and 24 μm emission maps used in our analysis of 8 face molecular gas and young stellar regions respectively.

APPENDIX B: MOLECULAR CLOUD LIFETIMES IN IC 342 AND M31

In order to derive absolute durations of the different phases of cloud evolution and star formation (see Section 3), we have used the cloud lifetime (t_{cl}) as a reference timescale. In our analysis, we focus on 46 of 50 CO-bright galaxies. For our sample, the cloud lifetime has been constrained in previous works using IR-selected face-on exposed star-forming regions. Here, we describe the characterization of the cloud lifecycle of IC 342 and M31, by applying the same method as described in Section 3 using 24 μm IR emission maps and face molecular gas and young stellar regions respectively.

Figure B1 shows the Hα emission maps of IC 342 and M31 used as face-on young massive star-forming regions. A summary of the observational data is presented in Section 2.1. Table B1 lists the adopted main input parameters. Specifically, for the analysis using CO and Hα as molecular gas and SFR tracers respectively, other input parameters are listed in Table 1 and Table 2. We set the minimum aperture size (r_{min}) to match the CO map resolution as it is coarser compared to the Hα map resolution (the reference timescale t_{cl} is set to the exposed young stellar phase duration, as the emission phase) are adopted from Hayden et al. (2020b). The duration loss to include the feedback timescale and the total duration of the Hα emission phase (t_{obs}) equals $t_{cl} + t_{fb}$.

In Figure B2 we show the measured deviations of the ratio of closest gas-to-SFR flux ratios in apertures centred on 3.6 μm Hα peaks compared to the galactic average together with our best-fitting model. Table 4 lists the constraints, uncertainties of the best-fitting model. We have verified the accuracy of these measurements in Section 3.1. We seek for our results using 24 μm IR as SFR tracer as well, using pixel-to-pixel correlation between gas and SFR tracer emission peaks. We measure cloud lifetimes of $20.0^{+1.0}_{-1.0}$ Myr for IC 342 and $14.0^{+0.5}_{-0.5}$ Myr for M31. The measured cloud lifetimes are within the range of our previous measurements in other galaxies where GMCs are found in isolation (8 – 30 Myr; Kruijssen & Longmore, 2014; Chevance et al. 2020b; Hygate 2020; Ward et al. 2020a; Zabel et al. 2020). We suspect that the difference between the two cloud lifetimes are related to the different environments in which the molecular clouds are located. It recently suggested by Chevance & Kruijssen (2020c) that in case the cloud evolution in IC 342, which has a high molecular gas surface density (9.55 $M_\odot$ pc^{-2}) is likely to be governed by galactic dynamical processes, whereas internal dynamics such as free-fall and crossing times are the determinant factor for cloud evolution in low molecular gas surface density en

In addition, most of these studies only constrain the duration of the zone dispersal after the young stars have become partially exposed. The exact role of or of different feedback mechanism remains ambiguous because the con duration of the embedded phase of star formation, including the heavily obscured phase, has not been quantified.

Studies of star-forming regions in the Milky Way and some nearby galaxies show that the embedded phase of massive star formation asts on $1 - 5$ Myr, where the duration of the heavily obscured phase is found to be $\sim 1.1 - 2$ Myr (Lada & Lada 2003; Whitmore et al. 2014; Corbelli et al. 2017). During the earliest stage of star formation, young massive stars are still embedded in their natal gas, as a result, the emission of heavily obscured, due to the extinction provided by the dust in dense gas surrounding the young stars. Despite this, on-going star formation is detectable using mid-infrared, hydrogen infrared, recombination lines, radio continuum emission, Lockman 1989; Kennicutt 1998a; Calzetti et al. 2005; Kennicutt et al. 2007; Crescent et al. 2007; Murphy et al. 2011; Vutisalchavakul & Evans 2013; Kerejeta et al. 2015). In particular, the 24 μm emission of the mid-infrared observed by the Multiband Imaging Photometer (MIPS) aboard the Spitzer Space Telescope provides an unbiased tracer of embedded massive star formation (e.g. see Kennicutt & Evans 2012 for review) at odds of the star-forming region are fully sampled within mass function, Vutisalchavakul & Evans 2013). 24 μm emission originates from stochastically heated small dust grains that do not require ionizing photons. It is excited, and empirically correlate with tracers of massive star formation are as far as used as a tracer of the presence of a large amount of hot, dust-reprocessed photospheric light from massive stars. Therefore, the 24 μm emission is assumed to trace only more massive stars are present. However, the radiation field from older stars (i.e. late-type B stars with an age of $\lesssim 100$ Myr) can make a non-negligible contribution to the dust heating and thus the mid-infrared dust emission (Draine & Li 2007; Verley et al. 2009; Leroy et al. 2012). The exact contribution at 24 μm wavelength is found to vary strongly between galaxies (e.g. 55% in M31 to Gaens et al. 2017, 90% in M33 to Williams et al. 2019) and up to a dozen, 40% within the galactic centre of the Milky Way (see Koepfer et al. 2013).

Following the theoretical model of star formation by Schmidt (1959), it is now observationally well-known that on galactic scales there is a tight correlation between the molecular gas surface density and the SFR surface density, the "star formation relation" (Schmidt 1997; Kennicutt 1998b; Bigiel et al. 2008; Leroy et al. 2013). However, this relation is also observed to break down on scales smaller than ~ 1 kpc (e.g. Onodera et al. 2010; Schruba et al. 2010; Sora et al. 2013; Leroy et al. 2013; Kreckel et al. 2018; Williams et al. 2018; Kruijssen et al. 2019; Schinnerer et al. 2019). This breakdown is caused by the small-scale de-correlation between GMCs and young stellar regions on sub-kpc scales and can be explained by assuming that individual regions in a galaxy follow independent lifecycles during which clouds assemble, form stars, and are disrupted by feedback (Schruba et al. 2010; Feldmann et al. 2011; Kruijssen et al. 2014; Longmore et al. 2014).

Kruijssen & Longmore (2014) and Kruijssen et al. (2018) developed a formalism that translates the observed de-correlation quantitatively into the evolutionary timeline of GMCs from cloud formation to subsequent star formation, and finally cloud dispersal. In brief, this method uses the spatial variation of the gas-to-SFR flux ratio observed at different spatial scales, ranging from cloud ~ 100 pc to galactic ~ 1 kpc scales or apertures placed at the gas peaks or SFR tracer peaks. These measurements are then used to determine the duration of each phase of the evolutionary cycle, the cloud lifetime, the timescale of SFR tracer is visible, and the phase during which both molecular gas and SFR tracers overlap, which represents the duration of massive star formation as well as the timescale for molecular gas to be removed by dissociated or feedback. This method does not rely on high angular resolution as much as previous methods, such as stellar tracer to relative fraction of GMCs with and without internal star formation activity. Since it only requires the mean separation length between regions undergoing independent evolution (100 ± 50 pc, Chevance et al. 2020c), it is resolved instead of resolving individual star-forming regions ($10 - 50$ pc, Kawamura et al. 2009).

This method has been used to characterise the evolutionary timeline between molecular gas and exposed young stellar populations using CO and Hα observations. The first applications of this method to a number of galaxies covering a large range of galactic environments (Kruijssen et al. 2019; Chevance et al. 2020a,c; Hygate et al. 2020; Ward et al. 2020a; Zabel et al. 2020) have shown that GMCs live for $10 - 30$ Myr. CO and Hα emission are found to be coincident on $1 - 3$ Myr during which time feedback from the young stellar population disperses the molecular gas in their birth clouds. Considering that supernova explosions are expected $\gtrsim 3$ Myr after massive stars are formed (Leitherer et al. 2014; Chevance et al. 2020a), the short duration of overlapping CO and Hα emission suggests that pre-supernova feedback such as photoionization and stellar winds is important for disrupting star-forming molecular clouds (Chevance et al. 2020b) and see Barnes et al. 2020; Ward et al. 2020b). have also used this method and extended the evolutionary timeline of star-forming regions by incorporating H emission of trace atomic gas. The measured atomic gas cloud lifetime of the LMC is ~ 50 Myr, and almost overlap with the exposed star-forming phase is detected.

In this paper we aim to apply further the characterisation of the GMC evolutionary lifecycle and use CO, 24 μm, and Hα emission as tracers of molecular gas embedded star formation and exposed star formation respectively for six nearby galaxies: IC 342, LMC, M31, M33, M51 and NGC 300). Previous applications of the statistical method of the same galaxies have focused on characterising the GMC lifecycle using CO emission as a tracer of the molecular gas and Hα emission as a tracer of the young massive stars (NGC 300: Kruijssen et al. 2019; M51: Chevance et al. 2020c; M33: Hygate et al. 2020) and the LMC (Ward et al. 2020a). We derive novel measurements of the GMC lifetimes of IC 342 and M31 in this paper, see Appendix B1 these are based on CO and Hα observations presented in Schruba et al. 2021a,b). Employing Spitzer 24 μm observations allows us to probe the earliest phase of star formation where the stars are still heavily obscured and quantify how long it takes young star-forming regions to emerge from their natal cloud at which point the H II regions creates a hole (ionizing radiation become visible).

The structure of this paper is as follows: in Section 1 and Appendix A, we describe the observational data used in our analysis. In Section 3, we summarise the statistical method used here and describe the associated input parameters for the galaxies in our sample. This is complemented in Appendix B where we present in more detail the application of this method to IC 342 and M31. In Section 4, we then present the derived duration of the embedded massive star-forming phase, which can be separated into heavily obscured phase of star formation and partially exposed phase of star formation based on the existence of Hα emission. The total duration of the 24 μm emitting phase is also presented. In addition, we explore how the durations of these phases vary with environ

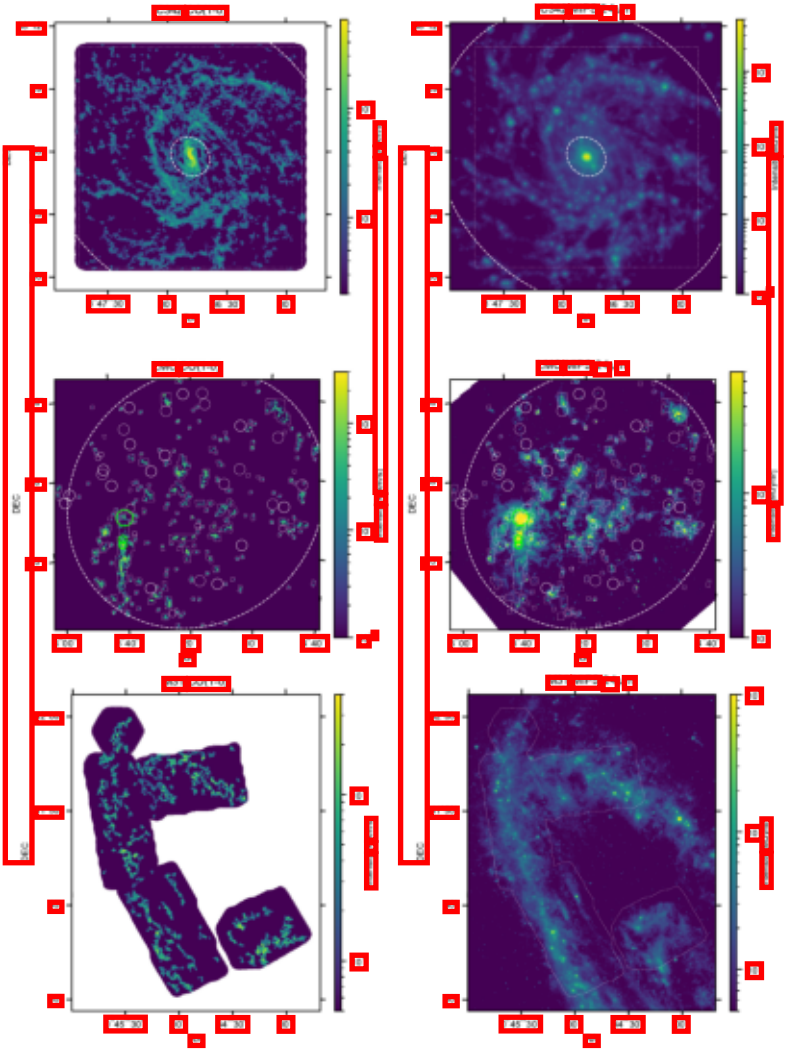

Figure A1. Maps of CO(1–0) emission (left panels) and 24 μm emission (right panels) for the IC 342, LMC, and M31. The ranges of galactic radii included in our analysis are indicated in white dashed ellipses. The white dotted lines show the coverage of the 4 observations of the LMC region when molecular cloud or wrong or artefact in the MAGPHIS survey or masks, while solid circles indicate masks made for foreground stars, background galaxies, and map artifacts (purple circles).

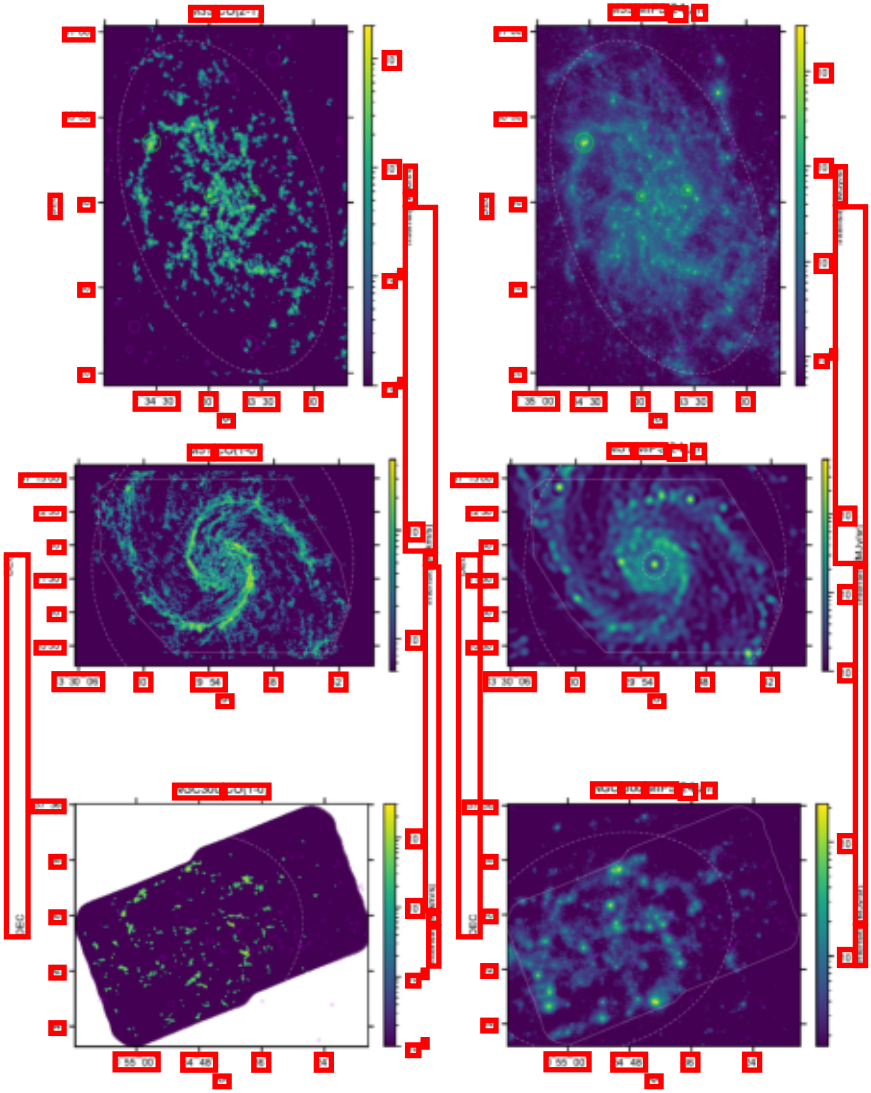

Figure A2. Same as Figure A1, but here for M33, M51, and NGC 300. Integrated intensity maps of CO(1–0) are shown for M51 and NGC 300, while CO(2–1) is shown for M33.

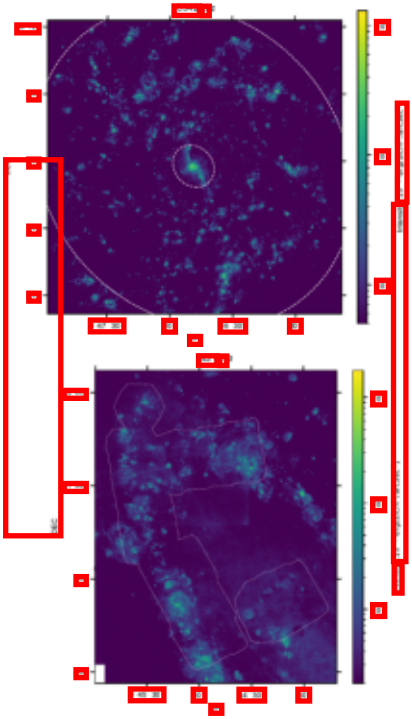

Figure B1. Same as Figure A2, for Hα emission maps of IC 342 and M31.

Table B1. Main input parameters of the analysis using Hα as an SFR tracer in IC 342 and M31. For other input parameters, we use the default values listed in table 2 of Kruijssen et al. (2019).

Quantity	IC 342	M31
$y_{\rm gal,min}$	[illegible]	[illegible]
$y_{\rm gal,max}$	[illegible]	[illegible]
[illegible]	[illegible]	[illegible]
$N_{\rm pix,min}$	[illegible]	[illegible]
$\Delta\log_{10}\tau$	[illegible]	[illegible]
$\log_{10}\tau_{\rm 0}$	[illegible]	[illegible]
$\log_{10}\tau_{\rm 1}$	[illegible]	[illegible]
$\log_{10}\tau_{\rm 2}$	[illegible]	[illegible]
$\tau_{\rm c}$ [Myr]	[illegible]	[illegible]
$\tau_{\rm ref,error}$ [Myr]	[illegible]	[illegible]
$\tau_{\rm ref,max}$ [Myr]	[illegible]	[illegible]
[illegible]	[illegible]	[illegible]

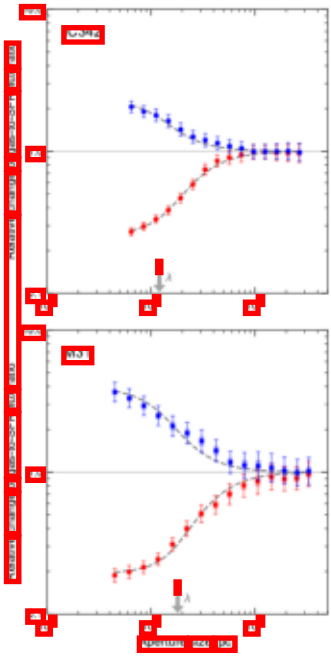

Figure B2. Relative change in the gas-to-SFR (CO-to-Hα) ratio with varying in galactic averages in (1) selection in size of apertures placed in M31 using the Hα emission scale (the red dot indicates the most fiducial, but non-Bayesian, choice) in which the uncertainty taking into account the covariance between data points. Our best-fitting model is shown as dashed lines and in the non-parametric and in galactic averages in measures error separation cases, as indicated in each panel in the constrained best-fitting parameters ($\tau_{\rm c}$ and $\tau_{0,\,1,\,2}$) are listed in Table 3.

Astronomisches Rechen-Institut, Zentrum für Astronomie der Universität Heidelberg, Mönchhofstraße 12-14, 69120 Heidelberg, Germany
Max-Planck-Institut für Extraterrestrische Physik, Giessenbachstraße 1, 85748 Garching, Germany
Center for Astrophysics and Space Sciences, Department of Physics, University of California, San Diego, 9500 Gilman Drive, La Jolla, CA 92093, USA
Argelander-Institut für Astronomie, Universität Bonn, Auf dem

Bugel, 11, 53121, Bonn, Germany
[1]The Observatories, 813 Santa Barbara Street, Pasadena, CA 91101, USA
[2]Departamento de Astronomía, Universidad de Chile, Casilla 36-D, Santiago, Chile
[3]AIM, Marseille, Univ. CNRS, CNES, CEA, Laboratoire d'Astrophysique de Marseille, Marseille, France
[4]Department of Physics & Astronomy, University of Wyoming, Laramie, WY 82071
[5]Department of Astronomy, University of Massachusetts, Amherst, 710 N. Pleasant St., Amherst, MA 01003
[6]Institut für Theoretische Astrophysik, Zentrum für Astronomie der Universität Heidelberg, Albert-Ueberle-Strasse 2, 69120 Heidelberg, Germany
[7]Research School of Astronomy and Astrophysics, Australian National University, Canberra, ACT 2611, Australia
[8]International Centre for Radio Astronomy Research, University of Western Australia, 35 Stirling Highway, Crawley, 6009, WA, Australia
[9]IRAM, 300 rue de la Piscine, 38406 Saint Martin d'Heres, France
[10]Universität Heidelberg, Interdisziplinäres Zentrum für Wissenschaftliches Rechnen, Im Neuenheimer Feld 205, 69120 Heidelberg, Germany
[11]Caltech/IPAC, MC 314-6, Keck Spalding Building, 1200 E California Blvd, Pasadena, CA 91125
[12]Department of Astronomy, The Ohio State University, 140 West 18th Ave., Columbus, OH 43210, USA
[13]Sorbonne Université, Observatoire de Paris, Université PSL, CNRS, LERMA, F-75005, Paris, France
[14]Observatorio Astronómico Nacional (IGN), C/Alfonso XII, 3, Madrid, E-28014, Spain
[15]Max Planck Institut für Astronomie, Königstuhl 17, 69117 Heidelberg, Germany

This paper has been typeset from a TEX/LaTeX file prepared by the author.

mental properties across the small galaxy sample for which these measurements are possible. We discuss the robustness of our results and compare them with the literature in Section 8. Lastly, we present our conclusions in Section 9.

2 OBSERVATIONAL DATA

We apply our analysis to six nearby galaxies (LMC, SMC, M31, M33, M51 and NGC 300) the size of our sample is mostly limited by the angular resolution of the *Spitzer* MIPS observations at 24 μm (~6.4″ Kieko et al. 2004) corresponding to 1.8 kpc at the galaxies of our sample including M33, for which we use a map of higher angular resolution (see Section 5.1). Also, the fact that we need to resolve at least the separation length between star forming regions (undergoing independent evolutionary lifecycles ~100–200 pc) to apply our analysis (see Section 5.1.1 and Kruijssen et al. 2019b). Here we provide a summary of the observational data used to trace the molecular gas emission (from low- and rare transitions), embedded massive stars (24 μm emission) and exposed young stellar regions (Hα emission). Composite three-color images of the SO, 24 μm and Hα maps are presented in Figure 1 whereas the individual SO and 24 μm maps are shown in Appendix A. The physical and observational properties of the galaxies in our sample are listed in Table 1.

2.1 Descriptions of multi-wavelength data sets

(CO 2-1) We adopt a distance of 3.43 Mpc (Wu et al. 2014) an inclination of 51.0° and a position angle of 22.0° (Meier et al. 2002). The adopted metallicity at the galactic centre is $12 + \log(O/H) = 8.85 \pm 0.04$, with a radial gradient of −0.0500 ± 0.0088 dex kpc^{-1} as measured by Pilyugin et al. (2014) using the strong-line counterpart method by Pilyugin et al. (2012). We use a combination of NOEMA and IRAM 30-m observations of the CO ($J = 1 - 0$) transition (denoted as CO 1–0) in the following, from Schruba et al. (2021a) as tracer molecular gas at (CO 2-1) covering out to 6.5 kpc of galactic radius. The final data cube has a circular beam size of 3.6″, a spectral resolution of 4.1 km s^{-1} and a sensitivity of 3.8 mK per 5 km s^{-1} velocity channel integrating over 1 km s^{-1}. This translates to a 1σ point source sensitivity of $\sigma(M_{\rm CO}) = 1.0 \times 10^{4}$ M$_\odot$ when the CO 1–0-to-H$_2$ conversion factor $\alpha_{\rm CO}$ is used (Table 1) is assumed. In order to trace embedded star formation, we retrieves *Spitzer* MIPS 24 μm maps from the Local Volume Legacy (LVL) survey (Dale et al. 2009). In addition to the procedure described in Dale et al. (2009), we mask foreground stars with 11 < r-band magnitude < 16 matching the star DR2 catalog (Gaia Collaboration et al. 2018) to avoid background galaxies for visual inspection of extended and non-circular sources. We then subtract background emission with a plane determined in a 0.5 kpc from the galactic centre where it is the optical radius of the galaxy determined from the Lyon Extragalactic Database (Paturel et al. 2003a,b) Makarov et al. (2014). The emission has been observed with the Mosaic imager of the Mayall 4-m telescope. We utilise calibrated narrow-band (for the R-band images kindly provided by Kimberly Herrmann, private communication). We post-process these images as described in Schruba et al. (2021a). Briefly, we subtract continuum emission from the for image mask Milky Way star from the Gaia DR2 catalog, subtract a sky background by fitting a 1st order polynomial plane of galactic radius > 0.5 kpc and correct for galactic extinction adopting $A(H\alpha) = 1.$ [illegible] that which is derived from $E(B-V) = 0.492$ mag (Schlafly & Finkbeiner 2011) and in

extinction curve with $k_{H\alpha} = 1.$ [illegible] (Cardelli et al. 1989). For all the maps used here, we do not attempt to correct for the internal extinction so that it traces exposed star-forming regions. The resulting CO map has an angular resolution of 0.85″. Due to limited coverage of the CO survey and blending of bright sources in the galaxy centre, we restrict our analysis to regions where CO observations have been made within galactic radii of 1.5 × r_{25} kpc (shown in Figure 1).

LMC: We adopt a distance of 50 kpc (Pietrzyński et al. 2019) an inclination of 32.0° and position angle of 168.0° (Kim et al. 1998). The adopted metallicity of the centre of the LMC is $12 + \log(O/H) = 8.35 \pm 0.03$ with a radial gradient of −0.0105 ± 0.0105 dex kpc^{-1} as measured by Lorbric et al. (2017) using direct measurements of electron temperatures T_e from spectra of H II regions (direct T_e-based method). We combine the CO 1–0 data presented in the same data release as the Magellanic Mopra Assessment (MAGMA; Wong et al. 2011, 2017) to trace molecular gas. MAGMA is a mapping survey of the LMC and SMC using the Mopra 22-m telescope of the Australia Telescope National Facility. For the LMC, the observations were conducted as a follow-up study of the NANTEN survey (Fukui et al. 2008) to arcmin-resolution previously identified molecular clouds (~164 in total). CO clouds will improve resolution in order to resolve the LMC (~11 pc) as in Figure 1 while dotted lines show the coverage of the MAGMA survey, the white circles indicate regions where molecular gas has been detected by the NANTEN survey but not further targeted with the MAGMA survey. We exclude these white circle regions where the more LMC exist from our analysis. However we still include other regions not observed by the MAGMA survey which might have diffuse and faint CO emission. We note that the inclusion of these sight lines not covered by the MAGMA survey should have a negligible impact on our results because diffuse and faint emission is eventually removed from our analysis through filtering process see Section 3.1. Moreover, the MAGMA survey covers more than ~80% of the total CO emission from the LMC observed by the NANTEN survey (Wong et al. 2011). The observed CO emission from the MAGMA survey also shows good agreement with the molecular gas mass produced using the continuum emission modelling (Jameson et al. 2016) indicating that we cover most of the emission from GMCs. The resulting angular resolution of the MAGMA CO data is 45″ and the sensitivity is 0.5 K per 0.52 km s^{-1} velocity channel integrating over 1 km s^{-1}. This translates to a 1σ point source sensitivity of $\sigma(M_{\rm CO}) = 1.0 \times 10^{3}$ M$_\odot$ assuming the [illegible] from Table 1. The *Spitzer* MIPS 24 μm image is from the SAGE project (Meixner et al. 2006) covering [illegible] of the galaxy. The continuum subtracted Hα map is from the Southern H-Alpha sky

[illegible] we extrapolate the distribution of each galaxy as to be close to same literature for the reddening ($E(B-V)$) or the extinction law when correcting for Galactic extinction. This is to follow what has been done previously for each galaxy, in our first applications of the statistical method using CO and 24 μm emission (e.g. Kruijssen et al. 2019; Chevance et al. 2020; Ansar et al. 2021; Ward et al. 2022a). Nevertheless, similarly to the CO 1–0-to-H$_2$ and SFR conversion factor see Section 5.3 for the choice of correction factor, but modifies the measurements of timescales in region separation length, but only the derived total SFR and the integrated star formation efficiency.

[illegible] visit the cloud catalogue from the NANTEN survey (Fukui et al. 2008) [illegible] 0.02 pc modelling the CO emission from the GMC that were not observed by MAGMA. We have shown that excluding these regions from our analysis has a negligible effect on our measurements.

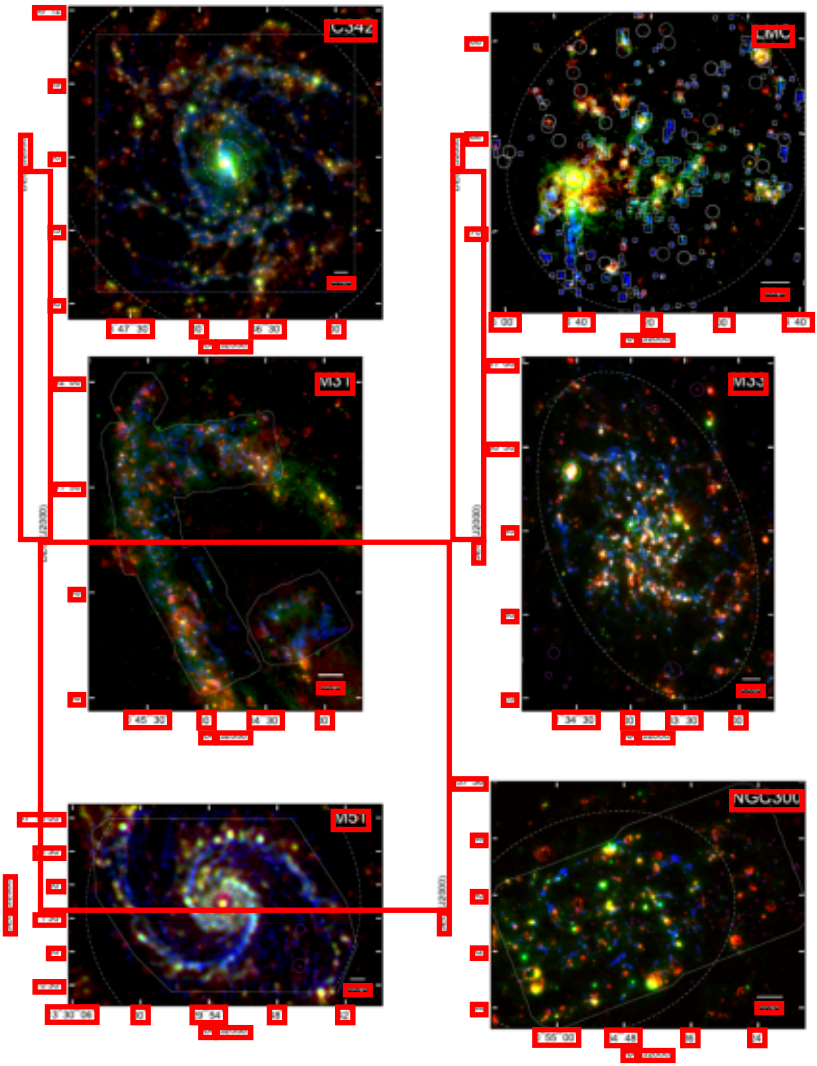

Figure 1. Composite three-color images of the six galaxies in our sample. The CO(1–0) emission (CO(2–1) for M51) is presented in blue, *Spitzer* MIPS 24 μm in green, and Hα in red. Galaxies are sorted by alphabetical order. The range of galactic radii included in the analysis is indicated by the white dashed ellipses. The inner ellipses of IC 342 and M51 show galaxy centres excluded from our analysis. The white dotted line shows the area where CO emission was observed. In each galaxy, excluding the right ascension sizes of its maps, its [illegible] is not shown in detail because it is outside the field of view. The massive star-forming region in the Orion Nebula in the LMC and NGC 300 in M33 is not in detail, which is masked. Bright stars are masked, which are excluded. M51 is the AGN region, but we do not exclude it. ALMA survey, so it is shown in red, so that it masked white with circles. Foreground stars that are not removed in the mapping extinction process and image artifacts are also masked (purple circles). A physical scale of 500 pc is shown in each image.

Table 1. Physical and observational properties of our galaxy sample.

galaxy	Stellar mass[a]	Metallicity[b]	Distance	Inclination	Position angle	CO observation	CO resolution	24 μm resolution	spatial resolution
	$10(g_0)$ $M_\odot$	$Z/Z_\odot$	Mpc	deg	deg		″	″	pc
N 346	0.2 ± 0.1	0.60 ± 0.20	6.8	44	251	SOFIA + IRAM 30-m	84	6	98
LMC N31 (NGC 224)	2.5 ± 0.1; 1.0 ± 0.1	0.48 ± 0.03; 0.76 ± 0.20	0.05; 0.78	23; 7.8	180; 37	APEX; CARMA + IRAM 30-m	26; 26	15; 15	4; 5
M33 (NGC 598); M31 (NGC 5194)	2.4 ± 0.1; 0.7 ± 0.1	0.50 ± 0.00; 1.37 ± 0.20	0.84; 8.4	52; 41	201; 153	IRAM 30-m; ARO + IRAM 30-m	8; 8	15; 15	8; 100
SGC 300	2.3 ± 0.1	0.48 ± 0.00	8.0	62	111	ALMA	0.5	15	8

[a] Adopted from Skibba et al. (2012) for the LMC and Sick et al. (2015) for M31, while others are from Leroy et al. (2019).
[b] CO luminosity-weighted metallicity over the considered field of view.
[c] Obtained using $Z/Z_\odot = [O/H]/(O/H)_\odot$, with the solar oxygen abundance $12 + \log(O/H)_\odot = 8.69$ (Asplund et al. 2009).
[d] Coarsest spatial resolution of the CO and 24 μm maps.

surveys, Atlas GALEX Nearby Galaxy Survey (NGS; Gil de Paz et al. 2007) has a spatial resolution of 4.2″. We correct for Galactic extinction using $A(H\alpha) = 0.16$ mag, which is derived from $E(B-V) = 0.06$ mag (Schlafly & Finkbeiner 2011) and an extinction curve with $R_V = 3.1$ (Cardelli et al. 1989). For the analysis here, we include emission from $0-3$ kpc in galactocentric radius, where the outer boundary is indicated in Figure 2.

M33. We adopt a distance of 0.78 Mpc (Dalcanton et al. 2012) and an inclination of 57.7° and a position angle of 77.7° (Corbelli et al. 2010). The adopted metallicity is the galactocentric gradient of $\log(O/H) = 8.36 - 0.027 \times R$ (kpc), with a radial gradient of -0.022 ± 0.014 dex kpc^{-1}, as measured by Zurita & Bresolin (2012) using the strong-line calibration from Pilyugin (2001) or, since molecular gas we use CO(1–0) data, as appeared in Lado-Fraile & Schruba (2016), with all details presented in Schruba et al. (2021b). The data is obtained as combination of CARMA interferometric data and IRAM 30-m data, the latter from Nieten et al. (2006). The CARMA observations cover the spiral arms of M33, a star forming disk of galactocentric radius of 4.5 kpc. Their native resolution of angular resolution of 5.5″ is spectral resolution of 0.05 km s^{-1} and sensitivity of 0.26 mK on the 43 m s^{-1} velocity channel integrating over 43 km s^{-1}. The translation of brightness temperature to surface density is $\Sigma(H_2)[M_\odot\,pc^{-2}] = 6.7 \times I_{CO}[K\,km\,s^{-1}]$ assuming the X_{CO} factor from table 10. We utilise the velocity masked moment-zero map, which is the signal of the flux-complete sample (see Schruba et al. 2021b for details). We employ the *Spitzer* MIPS 24 μm map presented in Gordon et al. (2006). This map is already background subtracted and we refer the reader to the original paper for more information on the data reduction procedure. The dust emission map is discussed in Schruba et al. (2021b) and has been created from calibrated narrow-band IR and K-band images from the Local Group Galaxies Survey (LGGS; Massey et al. 2006). The observations were carried out with the Mosaic imager of the Mayall 4-m telescope. The calibrated data were post-processed as described in Schruba et al. (2021b), which include the continuum subtraction masking of Milky Way stars using the same DR8 catalog Gaia collaboration et al. (2018) and sky background subtraction on rotating rings in plane of galaxy out to 30 kpc, and a correction for the contamination by [N II] by assuming that both N II lines contribute 45% to the total IR emission following Azimlu et al. (2011). The Galactic extinction is corrected by adopting a factor $A(H\alpha) = 0.14$ mag, which is derived from $E(B-V) = 0.05$ mag (Schlafly & Finkbeiner 2011) and a Galactic extinction curve with $R_V = 3.1$ (Cardelli et al. 1989). The resulting IR

map has an angular resolution of 1.5″. We perform our analysis in the sky plane as viewed by the CO observations.

M33. We adopt a distance of 0.84 Mpc (Gieren et al. 2013) an inclination of 55.08° and a position angle of 201.1° (Koch et al. 2018). The adopted metallicity is the galactocentric gradient of $\log(O/H) = 8.48 - 0.04 \times R$ (kpc), with a radial gradient of -0.042 ± 0.011 dex kpc^{-1}, as measured by Bresolin (2011) using the direct T_e-based method. We use the $^{12}CO(J=2-1)$ transition denoted as $CO(2-1)$ in the following data presented in Druard et al. (2014). Trace molecular gas the observations were carried out using the Heterodyne Receiver Array (HERA) of Schuster et al. (2004) on the IRAM 30-m telescope covering the galaxy out to a radius of 6 kpc. The resulting angular resolution is 12″, the average noise level is 54 mK per 2.6 km s^{-1} velocity channel integrating over 43 km s^{-1}. The noise level translates to a 3σ beam source sensitivity of $0.21 M_\odot\,pc^{-2}$ (assuming the X_{CO} from table 10). We retrieve *Spitzer* MIPS 24 μm image from the Local Volume Legacy (LVL) Survey (Dale et al. 2009). We then apply the same post-processing procedures as described above for IC 342. The narrow-band IR data is from Greenawalt (1998). The observations were carried out using the Burrell-Schmidt 0.6-m telescope of the Kitt Peak National Observatory (KPNO). Detailed information about the image reduction process can be found in Hoopes & Walterbos (2000). The Galactic extinction is corrected by using $A(H\alpha) = 0.1$ mag, obtained from $E(B-V) = 0.041$ mag (Schlegel et al. 1998) and an extinction curve with $R_V = 3.1$ (Fitzpatrick & Massa 2007). The resolution of the IR emission map is 8.0″. We restrict our analysis to galactocentric radii of 4 kpc as outlined in Figure 2.

M77. We adopt a distance of 8.0 Mpc (Jacobs et al. 2009) an inclination of 31.0° and a position angle of 173.0° (Colombo et al. 2014). The adopted metallicity is the galactocentric gradient of $12 + \log(O/H) = 8.88 \pm 0.053$ with a radial gradient of -0.0223 ± 0.003 dex kpc^{-1}, as measured by Pilyugin et al. (2014) using the strong-line "counterpart" method (Pilyugin et al. 2012). We use the $CO(1-0)$ data in the inner 10 × 4 kpc, as presented in Pety et al. (2013), as part of the PdBI Arcsecond Whirlpool Survey (PAWS; Schinnerer et al. 2013). The surveyed region is visible in Figure 1. The PdBI observations were carried out using A, B, and C configurations. The IRAM 30-m telescope was used to recover emission at low spatial frequencies. The final data have an angular resolution of 1.1″ and a sensitivity of 3.5 mK per 5 km s^{-1} velocity channel integrating over 43 km s^{-1}. The noise level trans

ates a 1 We point source sensitivity of $0.7\,M_\odot$ (3 km s^{-1} 10 K) assuming the 2 from table 1 the integrated intensity map was created by applying a mask of the data cube as described in Kim et al. (2023). Due to the limited resolution of our *Spitzer* MIPS 24 μm imaging (6.4″) Kieko et al. (2004) are still in principle only applying method 1 (galaxies closer than 5 Mpc) however using the higher resolution (2.4″) 24 μm map created by Dumas et al. (2011) we are able to expand the application of our method to M51, located at 8.6 Mpc. The map was created by applying the Richardson–Lucy deconvolution algorithm (Backus et al. 1968) to the all *Spitzer* infrared nearby galaxies survey (SINGS; Kennicutt et al. 2003) data. As we will see (Dumas et al. 2011) or more details). However we note that the artifacts introduced by the deconvolution algorithm could potentially bias our analysis especially on timescale-related quantities, by modifying the distribution of the 24 μm flux around bright peaks, limiting the interpretation of our results on this galaxy. The dust emission map is also from SINGS (Kennicutt et al. 2003). The observations were carried out using the KPNO 4-m telescope with the CCD imager. The map is corrected for galactic extinction adopting a correction factor of $A(H\alpha)/E(B-V) = 0.03$ map obtained from Schlafly & Finkbeiner (2011) adopt an extinction curve with $R_V = 3.1$ (e.g. Fitzpatrick 1999). We also correct for the contamination by N II lines by scaling the map by a factor of 0.7. The resolution of the dust emission map is 0.83″. Because we lack CO observations of the outer galaxy dust sources in the galaxy centre are affected by crowding and contamination from active galactic nucleus. We restrict our analysis to the field of view of the CO observations and within galactocentric radii of 0.51 – 5.3 kpc as indicated in Figure 1.

NGC 300. We adopt a distance of 2.0 Mpc (Dalcanton et al. 2009), an inclination of 42.0°, and a position angle of 111.0° (Westmeier et al. 2011). We adopt a metallicity of $12 + \log(O/H) = 8.46 \pm 0.05$ at the galactic centre and a radial gradient of -0.056 ± 0.015 dex kpc^{-1} as measured by Toribio San Cipriano et al. 2016 using a direct T_e-based method. We employ ALMA observations of the CO(1–0) transition from ALMA programmes 2013.1.00351.S (PI: A. Schruba) and 2015.1.00258.S (PI: A. Schruba) as presented in A. Schruba et al. in preparation and first used in Kruijssen et al. (2019). The observations were performed using the 12-m main array as well as the 7-m array and total power antennas of the ALMA Compact Array covering galactic radii out to 0.8 kpc. The resulting data have angular resolution of 2.1″ (~20 pc) and sensitivity of 1.1 K per 5 km s^{-1} channel, integrating over 0.5 km s^{-1}. The noise even translates a 1 K kpc^{-2} point source sensitivity of $0.7\,M_\odot$ (3 km s^{-1} 10 K) assuming the 2 from table 1. We retrieved *Spitzer* MIPS 24 μm image from the Local Volume Legacy (LVL) survey (Dale et al. 2009) and apply the same post-processing procedures as described above for NGC 3627. We use the dust image presented in Faes et al. (2014). This map is created from narrow-band dust and nearby continuum available in the ESO data archive and we use here the version kindly shared by Chris Faes (private communication). The observations were carried out with the Wide Field Imager (WFI) at the MPG/ESO 2.2-m telescope at La Silla Observatory. Correction for galactic extinction is applied using $A(H\alpha)/E(B-V) = 0.03$ map obtained from Schlafly & Finkbeiner (2011) and an extinction curve with $R_V = 3.1$ (Fitzpatrick 1999). We also account contamination by N II lines by assuming an intensity ratio $I(N\,II)/I(H\alpha) = 0.2$. The resolution of the map is 1.35″. In our analysis we consider emission from the field of view of the CO observations and within 1.8 kpc galactocentric radius (beyond which the molecular gas surface density drops precipitously) and the outer boundary is visible in Figure 1.

3.2. Homogenization of maps on common pixel grid

In order to apply our method the gas and SFR tracer maps of a given galaxy need to share the same pixel grid. Therefore, for each galaxy we regrid the map with a smaller pixel size to match the pixel size of the map with a larger pixel size. When the map that is being regridded has a better spatial resolution than the reference map, we first convolve the map with a Gaussian kernel to the resolution of the reference map before regridding to avoid introducing artifacts[1].

3.3. Construction of masks

We use the small-scale variation of the gas-to-SFR tracer ratio to constrain the evolutionary timeline of the molecular clouds (see Section 3.3). Definition of measurements are flux-weighted by images (see Kruijssen et al. 2018), which implies that very bright peaks dominate the significant fraction of the data and can bias our results. Therefore, we mask star-forming regions in the same galaxy as that are likely outliers of the luminosity function of SFR tracer peaks. Specifically, we first sort the peak pixel identifiers using CLUMPFIND (see Section 3.1) in descending order. We then look at the distribution by calculating the ratio of the flux between the nth brightest and the next brightest peak in line, starting from the brightest peak ($n = 1$). Defined as this ratio when the nth peak is more than twice as bright as the $(n+1)^{th}$ peak. Whenever this is found we mask all the peaks that are brighter than the $(n+1)^{th}$ brightest peak. As a result we mask three star-forming regions each in the LMC and in M33 before applying our analysis (green circles in Figure 1). These regions include 30 Doradus in the LMC and NGC 604 in M33, which alone contribute more than 80% of the 24 μm emission of each galaxy. Note that we would be masking the same peaks unless we slide down the brightness difference to 50% rather than 100% when defining the luminosity function of the case we would be masking one or four more peaks each in IC 342, M33 and NGC 300. The impact of masking such bright regions on the resulting derived parameters is generally small when averaging over the entire galaxy but becomes significant in the smaller fraction of the galaxy is considered, see Wang et al. 2020 for the effect of 30 Doradus on the LMC and Chevance et al. 2020c for the effect of the Headlight cloud in the Antennae galaxy NGC 628, also see Herrera et al. 2020. We also check for bright regions that satisfy the condition of the CO emission maps but could some finally we also mask artifacts in the maps (purple circles in Figure 1).

4. METHOD

We employ a statistical method (formalised in the Heidelberg code) to constrain the evolutionary timeline of GMCs. This timeline can be decomposed into the four lifetime the duration of the embedded phase of star formation (which continues until dispersal of molecular clouds) and the star formation traced lifetime. The characteristic separation length between star-forming regions (or complexes) independent evolution is also constrained by our analysis. Here we provide a summary of the methodology and the main input parameters. We refer the reader to Kruijssen & Longmore (2014) for a detailed explanation of the method. Kruijssen et al.

[1] When convolving the 24 μm map, we have also tested using a more exact kernel from Aniano et al. (2011) and found that the use of a Gaussian kernel has a negligible impact on our results.

2018) of the presentation and validation of the HERSCHEL code as well as the full set of input parameters and of a Chevance et al. (2020c) on general application of the method to nine nearby star-forming galaxies. The accuracy of the method has been demonstrated in Kruijssen et al. (2018) using simulated galaxies, and has since been confirmed through extensive observational tests performed in Kruijssen et al. (2019), Haydon et al. (2020a), Ward et al. (2020).

3.1 Description of the analysis method

Galaxies are composed of numerous GMCs and star-forming regions. The fundamental concept of our method is that stars do not independently undergoing their evolution from molecular clouds to the formation of stars. These evolutionary phases are observed using tracers e.g. CO and SFR tracers (e.g. Hα or 24 μm). We define the duration of each phase based on the resulting timescale of the tracers used. The timescale during which the emission tracer and the SFR tracer co-exist corresponds to the duration of massive star formation, thus the time it takes for the cloud to disperse molecular gas by stellar feedback, i.e. the feedback timescale, $\tau_{\rm fb}$ in the following. The cloud lifetime, $\tau_{\rm CO}$ denotes the time the star formation tracer lifetime is $\tau_{\rm SFR}$ = $\tau_{\rm fb}$ + $\tau_{\rm CO}$, the feedback timescale is $\tau_{\rm fb}$ = $\tau_{\rm SFR}$ − $\tau_{\rm CO}$, depending on the SFR tracer used.

During the initial phase of cloud evolution, (given independent region) only visible is the molecular gas tracer. As the cloud collapses and starts forming stars, the region becomes visible both in the gas and SFR tracers, eventually the remaining molecular gas is dispersed by stellar feedback and the region is only visible in the SFR tracers. Locally the gas-to-SFR flux ratio therefore increases with time during the evolution of a cloud. Observationally when focusing on a non-star-forming GMC, a higher gas-to-SFR flux ratio is measured compared to the large-scale ~1 kpc average gas-to-SFR flux ratio. By contrast, when focusing on a young star-forming region where most of the molecular gas has been dispersed, a lower gas-to-SFR flux ratio is measured. The deviations of the small-scale gas-to-SFR flux ratio compared to the large-scale average is a function of spatial scale can be directly related to the duration of the different phases of the GMC lifecycle (Kruijssen & Longmore 2014; Kruijssen et al. 2018).

In practice, as it is difficult to peak in the gas tracer and SFR tracer emission maps. We then convolve both maps into a range of spatial resolutions spanning from $\theta_{\rm min}$ to $\theta_{\rm max}$, see table 1. The minimum aperture size ($\theta_{\rm min}$) is set to a value that is close to the size of the major axis of the reprojected beam or the coarsest resolution between the two maps. Whereas the maximum aperture size ($\theta_{\rm max}$) covers most of the galaxy. For each convolved map aperture with the size of the corresponding resolution we placed at the identified gas and SFR tracer peaks. We then measure the gas and SFR tracer flux enclosed in these apertures to obtain the gas-to-SFR flux ratio as a function of aperture size. By fitting an analytical model describing the gas-to-SFR flux ratio as a function of the aperture size and its underlying evolutionary timescales we obtain a direct measurement of these timescales. This can be understood with an idealised example. For a tracer that is longer lived more peaks are typically identified, covering a larger fraction of the galaxy when small apertures are centred on them. Compared to the shorter-lived tracer. The measured flux ratio is therefore closer to the galactic average value of a longer-lived tracer than a shorter-lived one.

We use the analytical model derived by Kruijssen et al. (2018)

In the measurements, we also in order to constrain the relative duration of the different phases of the molecular cloud and star-forming region lifecycle, as well as the typical separation length between independent regions (L). The absolute duration of the different phases can then obtained by scaling the relative duration of timescales with a reference timescale ($\tau_{\rm ref}$). In our previous analyses using $\tau_{\rm CO}$ from observations (Kruijssen et al. 2019; Chevance et al. 2020; Hygate et al. 2020; Ward et al. 2020a) we used the duration of the isolated H II emitting phase ($\tau_{\rm H\,II}$) calibrated by Haydon et al. (2020b,a) using the stellar population synthesis model SLUG (de Mink et al. 2012; 2014; Krumholz et al. 2015) as the reference timescale. Here, in order to obtain absolute values when applying our analysis to CO and 24 μm maps we first apply the method to CO and Hα observations. This is to obtain the cloud lifetime, $\tau_{\rm CO}$ and its upward and downward uncertainties ($\tau_{\rm CO,upper}$ and $\tau_{\rm CO,lower}$), see table 1, which are adopted as the reference timescale ($\tau_{\rm ref}$) and its uncertainties ($\tau_{\rm ref,upper}$ and $\tau_{\rm ref,lower}$) in the analysis with CO and 24 μm observations. This fitted model has three independent and non-degenerate quantities ($\tau_{\rm Spitzer}$, $\tau_{\rm 24\,\mu m}$, and A). The best-fitting values are then obtained by minimising the reduced-χ^2 over these three quantities. The uncertainties of each parameter are propagated consistently throughout the analysis.

In the presence of diffuse emission can cause measurements by adding a large-scale component that is not associated with the identified peaks. This large-scale emission potentially includes the gas emission originating from sources related to the recent massive star formation such as low mass molecular clouds, ionised positive H II regions and ionizing photons that have escaped from H II regions (e.g. Wood et al. 2010; Belfiore et al. in preparation), it may also originate from other mechanisms not related to recent massive star formation, for example diffuse molecular gas, infrared emission powered by stars in intermediate age and diffuse ionized gas heated by shocks (Martin 1997; Ceron et al. 2021). We remove such diffuse emission in both gas and SFR tracer emission maps iteratively using the method presented in Hygate et al. (2019) which makes the derived timescales sensitive only to the massive/luminous molecular clouds and young stellar populations. This method filters emission on spatial scales larger than a given typical distance between regions, as measured from the HERSCHEL code using a Gaussian high-pass filter in Fourier space, for each galaxy we adopt the smallest possible value of L while ensuring the flux loss from the compact emission is less than 10% also following Chevance et al. (2020b); Hygate et al. (2020). See table 1. We in the adopted filtering scale because we want to maximise the removal of diffuse emission while minimising the impact of the filtering on the compact regions. The influence of L on the derived timescales is fully described in Hygate et al. (2019) and Hygate et al. (2020). A summary the choice of L does not significantly change the best-fitting model parameters as long as the adopted L is smaller than 30 and the flux loss from the compact emission is less than 10%. After the diffuse emission is filtered, pixels with noise mask with a threshold of twice the standard deviation noise level in the emission map is applied. We repeat this process until the convergence condition is reached which is when the changes of the measured values are less than 5% over three consecutive iterations.

3.2 Input parameters

Unless otherwise noted here we adopt the same parameters as in previous analyses using M51 as an SFR tracer, see Appendix A of Chevance et al. (2020). For the GMC, Hygate et al.

Table 2. Input parameters for the analysis using 24 μm as SFR tracers for each galaxy. Other parameters not mentioned here are the same as used in previous analysis using Hα as an SFR tracer.

Quantity	IC 342	M66	M33	M55	M51	NGC 300	Description
$a_{0,min}$ (pix)	10	10	10	10	10	10	Minimum aperture size to convolve the input maps to
$a_{0,max}$ (pix)	300	300	300	300	300	300	Maximum aperture size to convolve the input maps to
N_a	8	8	8	8	8	8	Number of aperture sizes used to create array of logarithmically-spaced aperture size in the range $(a_{0,min}, a_{0,max})$
$N_{pix,min}$	10	10	10	10	10	100	Minimum number of pixels for a valid peak
$\Delta\log_{10}\Sigma_{ini}$	0.1	0.1	0.1	0.1	0.1	0.1	Logarithmic range below flux maximum covered by flux contour levels for molecular gas peak identification
$\delta\log_{10}\Sigma_{ini}$	0.05	0.05	0.05	0.10	0.05	0.10	Logarithmic interval between flux contour levels for molecular gas peak identification
$\Delta\log_{10}\Sigma_{frac}$	0.1	0.1	0.1	0.1	0.1	0.1	Logarithmic range below flux maximum covered by flux contour levels for SFR tracer peak identification
$\delta\log_{10}\Sigma_{frac}$	0.05	0.05	0.05	0.10	0.05	0.10	Logarithmic interval between flux contour levels for SFR tracer peak identification
τ_{ref} (Myr)	20.0	20.0	20.0	20.0	20.0	20.0	Reference timescale spanned by molecular gas tracer
$\delta\tau_{ref,down}$ (Myr)	0.5	0.5	0.5	0.5	0.5	0.5	Downwards uncertainty on reference timescale
$\delta\tau_{ref,up}$ (Myr)	0.1	0.1	0.1	0.1	0.1	0.1	Upwards uncertainty on reference timescale
SFR ($M_\odot yr^{-1}$)	0.93	0.14	0.011	0.16	0.36	0.085	Total SFR in the analysed area
δ(SFR) ($M_\odot yr^{-1}$)	0.15	0.03	0.008	0.02	0.02	0.015	Uncertainty of the total SFR
$\log_{10}$ α_{CO}	0.63	0.63	0.66	0.63	0.66	0.63	Logarithm of CO(1–0)-to-H$_2$ conversion factor
$\delta\alpha_{CO}/\alpha_{CO}$	0.5	0.5	0.5	0.5	0.5	0.5	Relative uncertainty of α_{CO}
σ	1	1	1	1	1	1	Characteristic width for the Gaussian filter used to remove diffuse emission in Fourier space

M33, Chevance et al. 2020; or M51 and Kruijssen et al. 2019; or NGC 300). The parameters not mentioned here include distance, inclination, position angle (see Table 1), as well as parameters related to the fitting process and error propagation, for which default values are adopted as listed in Kruijssen et al. (2018). We use CLUMPFIND (Williams et al. 1994) to identify gas and SFR tracer peaks in each map. This algorithm finds peaks by drawing closed contours at a series of flux levels within a given flux range ($\Delta\log_{10}\Sigma$) below the maximum flux level with an interval of $\delta\log_{10}\Sigma$ between flux levels. The adopted values for our samples are summarised in Table 2. Moreover, it rejects identifying point sources that are likely to be foreground stars that were not masked during the mask creation process or externally illuminated surfaces (see Section 2.3). We only accept peaks that contain more than $N_{pix,min}$ pixels. The area of a $N_{pix,min}$ pixels equals $1.2 - 3.5$ times the coarsest beam size. We note that our choices of $\Delta\log_{10}\Sigma$, $\delta\log_{10}\Sigma$, $N_{pix,min}$, and σ do not affect our measurements significantly as long as peaks that are obviously visible in the emission maps have been identified. Kruijssen et al. (2018) explained above, and the uncertainties determined from our analysis with 5.0 and 10.0 are used as lower and upper bounds of the reference timescales (τ_{ref}). However, since we additionally mask out some of the bright star-forming regions for the reasons explained in Section 2.3, we re-run the same analysis using only the SFR tracer with updated masks. Our measurements using Hα and 24 μm SFR tracers are listed in Table 3 and are in very good agreement with or identical to the previously published results for the analysis with 5.0 and 24 μm. τ_{ref} includes the feedback phase. The $CO(1-0)$-to-H$_2$ conversion factor (α_{CO}) including the contribution from heavy elements) is adopted from Bolatto et al. (2013) expressed as

$$\alpha_{CO} = 2.0 \times 10^{20}\ \mathrm{cm^{-2}\,(K\,km\,s^{-1})^{-1}} \times \exp\left(\frac{0.4\,Z'}{Z_\odot}\right), \quad (1)$$

We adopt the metallicity-dependent part but not the surface density dependence from Bolatto et al. (2013). For simplicity, we adopt a constant α_{CO} value for each galaxy and a conservative uncertainty of 50% in addition to M33, which is the only galaxy with $CO(2-1)$ data, we adopt a fixed ratio of $CO(2-1)/CO(1-0)$ of 0.8 (Leroy et al. 2009). Finally, we derive the total SFR of the maps using the combined 24 μm and Hα emission maps and using the conversion factor from Calzetti et al. (2007), expressed as

$$\mathrm{SFR(M_\odot\,yr^{-1})} = 5.3 \times 10^{-42}\,[L(\mathrm{H}\alpha) + 0.031\,L(24\,\mu\mathrm{m})], \quad (2)$$

where the luminosities have units of erg s^{-1} and $L(24\,\mu\mathrm{m})$ is expressed as $\nu L(\nu)$. We assume a typical uncertainty of 30% on the derived SFR. These conversion factors are only used to derive additional physical quantities such as the molecular gas surface density and the integrated star formation efficiency. We note that the exact values of these conversion factors, unless they vary spatially, do not affect our measurements of primary quantities, which are the durations of the successive phases of cloud evolution and star formation, or as they affect the region separation length between independent regions.

3 RESULTS

3.1 The molecular cloud lifecycle

Here, we present our results from the application of our method to the maps of CO and 24 μm emission presented in Section 2 for the tracers of the molecular gas and the SFR of six nearby galaxies. Figure 2 shows the gas-to-SFR flux ratios measured around gas and SFR tracer peaks as a function of aperture size together with our best-fitting models of each galaxy, going toward smaller aperture sizes from left to right. The measured flux ratios of both tracers increasingly deviate from the galactic average, illustrating the spatial de-correlation between the gas and SFR tracer emission peaks. Table 3 summarises the constrained best-fitting values from applying our analysis to the Hα and CO maps as well as the 24 μm and CO maps. The first experiment allows us to measure τ_{ref}, which is the used as the reference timescale in the second experiment (see Section 3.3 Table 1 also lists other physical

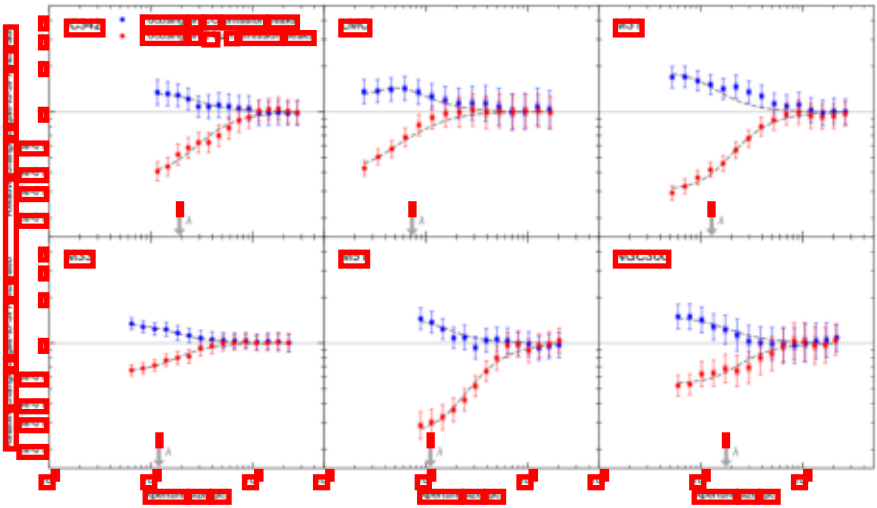

Figure 7. Relative changes in the gas-to-SFR (CO-to-24 μm) flux ratio compared to the galactic average as a function of the H2 or H surface density. Blue (red) 24 μm (CO) emission scales are error bars indicate the uncertainty of each individual datapoint, while shaded areas show the effective uncertainty taking into account the covariance between data points. The galactic average is shown as the solid horizontal line in the panels, and indicates the best-fitting model. The constraints (error separation length ℓ) indicated in each panel, with the downward arrow on the other constraints, best-fitting parameters ($t_{\rm fb,24\,\mu m}$ and $t_{24\,\mu m}$) are listed in Table 3.

Table 3. Physical quantities constrained using the method described in Section 3, describing the evolution of molecular clouds to exposed or embedded stellar populations traced by Hα and 24 μm, respectively, following the rotation throughout the upper $\sigma_{\rm v}$. τ is the total lifetime, $t_{\rm fb,H\alpha}$ and $t_{\rm fb,24\,\mu m}$ are the duration of the partially exposed and embedded star-forming phase, respectively, and $t_{\rm H\alpha}$ and $t_{24\,\mu m}$ are the duration of Hα and 24 μm emitting phase, respectively. The region separation length (ℓ) measured with different SFR tracers, feedback velocity ($v_{\rm fb}$), and star-formation efficiency ($\epsilon_{\rm ff}$) are also listed.

	CO vs Hα				CO vs 24 μm				
galaxy	τ	$t_{\rm fb,H\alpha}$	$t_{\rm H\alpha}$	ℓ	$t_{\rm fb,24\,\mu m}$	$t_{24\,\mu m}$	ℓ	$v_{\rm fb}$	$\epsilon_{\rm ff}$
	Myr	Myr	Myr	pc	Myr	Myr	pc	km s^{-1}	per cent
LMC	$10.0^{+2.0}_{-2.0}$	$1.5^{+0.0}_{-0.0}$	$1.6^{+0.0}_{-0.0}$	$20^{+0.0}_{-0.0}$	$3.7^{+1.8}_{-1.8}$	$7.0^{+1.8}_{-1.8}$	$90^{+0.0}_{-0.0}$	$14^{+0.0}_{-0.0}$	$1.0^{+0.0}_{-0.0}$
SMC	$1.1^{+0.0}_{-0.0}$	$1.5^{+0.0}_{-0.0}$	$1.6^{+0.0}_{-0.0}$	$8^{+0.0}_{-0.0}$	$0.0^{+0.0}_{-0.0}$	$8.6^{+0.0}_{-0.0}$	$5^{+0.0}_{-0.0}$	$0.0^{+0.0}_{-0.0}$	$3^{+0.0}_{-0.0}$
M33	$14.0^{+2.0}_{-2.0}$	$1.5^{+0.0}_{-0.0}$	$1.6^{+0.0}_{-0.0}$	$81^{+0.0}_{-0.0}$	$3.4^{+1.8}_{-1.8}$	$5.3^{+1.8}_{-1.8}$	$256^{+0.0}_{-0.0}$	$92.5^{+0.0}_{-0.0}$	$1^{+0.0}_{-0.0}$
M33	$4.5^{+0.6}_{-0.6}$	$1.5^{+0.0}_{-0.0}$	$1.6^{+0.0}_{-0.0}$	$55^{+0.0}_{-0.0}$	$3.3^{+0.8}_{-0.8}$	$1.9^{+0.8}_{-0.8}$	$190^{+0.0}_{-0.0}$	$10.3^{+0.0}_{-0.0}$	$3^{+0.0}_{-0.0}$
M33	$10.3^{+1.0}_{-1.0}$	$1.5^{+0.0}_{-0.0}$	$1.6^{+0.0}_{-0.0}$	$40^{+0.0}_{-0.0}$	$3^{+1.0}_{-1.0}$	$2.6^{+0.0}_{-0.0}$	$3^{+1.36}_{-1.36}$	$2^{+0.0}_{-0.0}$	$3^{+0.0}_{-0.0}$
SGC-90	$10.8^{+2.0}_{-2.0}$	$1.5^{+0.0}_{-0.0}$	$1.6^{+0.0}_{-0.0}$	$10^{+0.0}_{-0.0}$	$3.9^{+1.8}_{-1.8}$	$1.9^{+1.8}_{-1.8}$	$0.75^{+0.0}_{-0.0}$	$0^{+0.0}_{-0.0}$	$3^{+0.0}_{-0.0}$

[a] Only a 1σ upper limit can be derived for not satisfying (ii) and (vii) in Section 5.1.1.

quantities, which can be derived from our measurements, such as the feedback outflow velocity ($v_{\rm fb}$; see section 5.1.5) and the inter-trates cloud-scale star formation efficiency ($\epsilon_{\rm ff}$; see Section 5.1.4). In Figure 8 we show an illustration of the evolutionary timelines of molecular clouds and star-forming regions in our galaxy sample. GMCs initially emit only in CO, then in 24 μm after the onset of star formation and finally in Hα when the star-forming regions become partially exposed.

5.1.1 Feedback timescale

The use of 24 μm emission enables us to take the heavily obscured phase of star formation into account, which cannot be done with